



HAL
open science

Examination of crystal dissolution in 3D: A way to reconcile dissolution rates in the laboratory?

Catherine Noiriél, Matthias Oursin, Damien Daval

► To cite this version:

Catherine Noiriél, Matthias Oursin, Damien Daval. Examination of crystal dissolution in 3D: A way to reconcile dissolution rates in the laboratory?. *Geochimica et Cosmochimica Acta*, 2020, 273, pp.1-25. 10.1016/j.gca.2020.01.003 . hal-03010602

HAL Id: hal-03010602

<https://hal.science/hal-03010602>

Submitted on 17 Nov 2020

HAL is a multi-disciplinary open access archive for the deposit and dissemination of scientific research documents, whether they are published or not. The documents may come from teaching and research institutions in France or abroad, or from public or private research centers.

L'archive ouverte pluridisciplinaire **HAL**, est destinée au dépôt et à la diffusion de documents scientifiques de niveau recherche, publiés ou non, émanant des établissements d'enseignement et de recherche français ou étrangers, des laboratoires publics ou privés.

1 Examination of crystal dissolution in 3D: a way to
2 reconcile dissolution rates in the laboratory?

3 Catherine Noiriel^{1,*} Matthias Oursin¹, and Damien Daval²

4

5 ¹Géosciences Environnement Toulouse, Observatoire Midi-Pyrénées, Université Paul Sabatier,
6 CNRS, IRD, Université de Toulouse, 14 avenue Edouard Belin, F-31400 Toulouse, France.

7 ²Laboratoire d'Hydrologie et de Géochimie de Strasbourg, Université de Strasbourg, EOST,
8 CNRS, 67084 Strasbourg, France.

9

10

11 * corresponding author

12

13

14

15

16

17 KEYWORDS

18 Calcite dissolution, X-ray micro-tomography, 3D crystal geometry, dissolution rate
19 distribution, surface topography, rate mapping, rate variability, face-specific dissolution, edge
20 contribution

21

22 HIGHLIGHTS

23 Determination of the local rates of dissolution of a whole calcite crystal in 3D

24 Etch pits progressively annihilate and disappear as far as dissolution progresses

25 Contribution of calcite crystal faces, edges and corners to dissolution are evaluated individually

26 Crystal edges progressively control the dissolution at the crystal scale

27 Contribution of the edges to the overall dissolution is crystal size and time dependent and was
28 evaluated through a simple geometric model.

29 The technique is limited by imaging resolution but has no limited depth of investigation at the
30 crystal surface

31

32 ABSTRACT

33 Surface reactivity is a major parameter controlling mineral reactivity, and microscopic
34 techniques investigating surface retreat with time have pointed at the heterogeneous and/or
35 anisotropic reactivity of minerals, in relation with the diversity and stochastic distribution of
36 energetic sites. However, in view of the discrepancies between rates determined in the
37 laboratory, a thorough 3D approach of a whole crystal reactivity might be particularly attractive
38 to evaluate the respective contributions of single faces and crystal edges to the dissolution flux,
39 and to fill the gap between the rates derived from face-specific, topography observations at
40 micro-scale (i.e., with no contribution of the edges to dissolution) and those determined on

41 crystal powders in continuously stirred reactors (with an overcontribution of the edges and
42 surface defects to dissolution). Here, we provide a detailed 3D characterization of the geometry
43 evolution and dissolution rate of a single crystal of calcite at pH 4.5 and 4.0 using X-ray micro-
44 tomography (XMT) with a pixel size of 0.325 μm . Evaluation of the retreat and mapping of the
45 reaction rates at the 3D crystal surface reveals a large range of dissolution rates reflecting the
46 specific contributions of the different regions of the crystal. During dissolution and against all
47 expectation, etch pits forming at the crystal surface progressively annihilate, primarily by
48 intersecting with trains of steps coming from the near edge regions. The global rate determined at
49 the crystal scale integrates the contribution of the local rates of all the crystal features, with \bar{r}'_{corner}
50 $> \bar{r}'_{edge} > \bar{r}'_{cleavage} > \bar{r}'_{macrostep} \sim \bar{r}'_{pit} > \bar{r}'_{macrostepbase}$. Crystal rounding reveals that contribution from
51 the crystal edges progressively dominates the dissolution process over pit formation at the
52 $\{10\bar{1}4\}$ surfaces. The contribution of the edges to dissolution increases the crystal dissolution
53 rate by at least 1.6 to what would be a face-specific dissolution, and will be size- and time-
54 dependent, as suggested by a simple geometric model based on uniform or non-uniform
55 dissolution of the faces of a model crystal. Finally, comparison of the method to vertical
56 scanning interferometry measurements and scanning electron microscopy observations on
57 surface portions shows that XMT imaging is robust, suggesting that its application to the
58 dissolution/precipitation of other minerals would be highly beneficial to determine reliable rates
59 that can be further used to model mineral reactivity.

60

61 1. INTRODUCTION

62 Mineral reactivity is fundamentally important in Earth sciences, as it controls many of the natural
63 or anthropogenic geochemical processes, such as continental weathering, diagenesis,
64 hydrothermal alteration, carbon dioxide sequestration, nuclear waste disposal, groundwater
65 contamination, or geothermal energy production (Depaolo and Orr, 2008; Kump et al., 2000;
66 Morse and Arvidson, 2002; Noiriél and Daval, 2017; Steefel et al., 2005). In this regard, a
67 specific attention has been paid over a century to the determination of reliable kinetic rate laws,
68 with the ultimate goal to better understand, quantify and predict chemical transformations and
69 mass transfers over large space and time scales. However, bridging the gap between rates

70 measured in the field and determined in the laboratory remains an elusive objective, when
71 already discrepancies exceeding largely the analytical errors have long been reported between
72 reaction rates determined in the laboratory, despite the well-controlled physicochemical
73 conditions of the experiments (Fischer et al., 2014). This aspect points towards an intrinsic
74 variability of mineral reactivity, all extrinsic factors being equal, which must be characterized
75 and understood to ultimately upscale laboratory-derived rates to natural settings.

76 Intrinsic sources of variation have been highlighted through the measure of the distribution of
77 local rates at the crystal surface (Fischer et al., 2012), which can be treated in the framework of
78 the so-called “rate spectra” concept, and reflect the heterogeneous distribution of defects
79 outcropping at the crystal surface. Therefore, it is not surprising that bulk dissolution rate data
80 obtained from reactor experiments on crushed crystals (i.e., mineral powders) differs from
81 dissolution rate data measured locally at the surface of polished or pristine crystals, due to
82 differences in surface reactivity distribution at the two scales of observation, and also because
83 sample preparation may play a key role in the resulting distribution of reactive sites. Surface
84 reactivity, which is ultimately dependent on three parameters, i.e., chemical composition, atomic
85 structure and fine-scale morphology (Hochella, 1990), can exert a crystallographic or
86 microstructural control of mineral reactivity (Daval et al., 2013; Pollet-Villard et al., 2016a;
87 Saldi et al., 2017). In this regard, microscopic techniques measuring the topography at the fluid-
88 mineral interface are particularly attractive to investigate mineral reactivity.

89 Changes at the mineral surface can be evaluated *in situ* or *ex situ* by measuring the vertical
90 retreat under various experimental conditions with micrometer to nanometer resolutions using
91 methods such as atomic force microscopy (AFM) (Emmanuel, 2014; Hillner et al., 1992; Jordan
92 and Rammensee, 1998; Shiraki et al., 2000; Stipp et al., 1994), vertical scanning interferometry
93 (VSI) (Fischer and Lutge, 2007; Smith et al., 2013), phase shifting interferometry (PSI) (Ueta et
94 al., 2013), confocal profilometry (Godinho et al., 2012), X-ray reflectivity (Fenter et al., 2000),
95 digital holographic microscopy (DHM) (Brand et al., 2017) or X-ray microscopy (Laanait et al.,
96 2015). Such methods have enabled measurements of dissolution rates on face-oriented single
97 crystals or polycrystalline aggregates, and evidenced their variability at the mineral surface, with
98 heterogeneous and/or anisotropic reactivity reflecting the energetic diversity of reactive sites. For
99 instance, application of these techniques to the study of cleaved $\{10\bar{1}4\}$ surface of calcite has

100 provided insightful observations of the contribution of etch pits and step retreat, or their
101 interactions, to dissolution under a large variety of experimental conditions (Arvidson et al.,
102 2006; Arvidson et al., 2003; Hillner et al., 1992; Shiraki et al., 2000; Smith et al., 2013
103 Bouissonnié et al., 2018; Duckworth and Martin, 2004; Jordan and Rammensee, 1998; Miyata et
104 al., 2017; Ruiz-Agudo et al., 2009; Teng, 2004; Xu et al., 2010). Fine-scale observations at the
105 crystal surface have also contributed to challenge the conventional treatment of reaction kinetics
106 from mineral powders that has prevailed so far, which relies on the paradigms of homogeneity,
107 isotropy and immutability (Noiriel and Daval, 2017) and on the definition of a unique reaction
108 rate (Fischer et al., 2012).

109 However, these methods are often restricted to small observation surfaces (typically of areas less
110 than $500 \times 500 \mu\text{m}^2$). In addition, they often require the surface to be well cleaved or polished to
111 provide surfaces as flat as possible, inherent to a limited vertical range (e.g., about $5 \mu\text{m}$ for
112 AFM, but up to $150 \mu\text{m}$ for VSI). Consequently, they are often restricted to areas of lower
113 reactivity (Dove and Platt, 1996) and ignore the contribution of surface macro-patterns and
114 crystal edges. It has been pointed out that the missing contribution of the crystal edges and
115 corners to the calculation of reaction rates could explain lower rates obtained from VSI
116 measurements compare to bulk rate determination (Lüttge et al., 2003; Saldi et al., 2017).
117 Although it has long been assumed that crystal edges provide a source of reactive sites (Schott et
118 al., 1989), it is only very recently than the quantitative contribution of crystal edges to
119 dissolution rates has been evaluated experimentally (Noiriel et al., 2019), using X-ray micro-
120 tomography imaging (XMT). By enabling true 3D space, XMT should permit a significant
121 extension to current methods and models by singling out the reactivity of crystal corners and
122 edges, and to fill the gap between fine-scale (nm- to μm -scale) measurements of surface
123 reactivity and macroscopic determination of bulk rates on powders.

124 In this study, we have quantified the dissolution rate of a whole crystal of calcite at pH 4.0 and
125 4.5 by providing a direct measurement of the surface retreat rates at the crystal surface using 3D
126 XMT. We illustrate the heterogeneous distribution of the dissolution fluxes of the reacted crystal
127 through time from almost 7.5 million data points analyzed at the crystal surface. The objective is
128 to track the whole crystal topography at different time intervals in order to evaluate the
129 contribution of the different surface and crystal features to the reaction rate distribution. In

130 particular, we have evaluated the specific contributions of the crystal faces and edges on the long
131 term, i.e., for an average surface retreat of 22.4 μm . The robustness of the method is discussed by
132 comparing the crystal volume changes to chemical analyses of the calcium released during
133 dissolution, and the 3D imaging of the crystal surface to vertical scanning interferometry and
134 scanning electron microscopy (SEM) observations. As will be shown, the crystal edges play a
135 major role in the dissolution process, which is quantitatively assessed. The average rates, which
136 are in between the range of values reported for studies measuring the surface topography and
137 those derived from experiments on mineral powders can be considered as more representative for
138 dissolution of calcite cements (i.e., sub-mm crystals) in nature.

139

140 2. MATERIAL AND METHODS

141 2.1. Sample preparation

142 A single calcite crystal about 1.8 mm long and 0.6 mm wide was obtained after crushing and
143 sieving a cm-sized single spar crystal. The crystal was mounted on a glass capillary tube
144 (Hilgenberg, 400 μm O.D.) using epoxy resin, which covers the bottom face of the crystal
145 creating a mask that preserves it from dissolution. The crystal faces were not polished before the
146 experiment, so that the different faces are not perfectly cleaved and they exhibit various macro-
147 features such as ragged or curved cleavage macrosteps, hillocks, or rippled surface patterns,
148 which are inherited from the breaking and size reduction of the original calcite sample (see
149 further in Figure 3). In particular, three of the four side faces (further named face 1, 2, and 4)
150 exhibit well cleaved portions of surface along the $\{10\bar{1}4\}$ planes. Surface defects and
151 macrosteps intersecting the aforementioned planes are visible, as well as, for face 1, macrosteps
152 oriented along $\{01\bar{1}8\}$ parting planes. In contrast, the fourth side face (further named face 3) has
153 a 5° miscut angle with respect to the $\{10\bar{1}4\}$ plane, and is dominated by macrosteps and rippled
154 surface patterns. The top part of the crystal (further named face 5) is highly rough and stepped
155 with many $\{10\bar{1}4\}$ plane intersects. Some defects of limited extension such as micro-fractures
156 and cleavages are also noticed inside the crystal, as a few micro-particles at the crystal surface.

157 2.2. Dissolution experiment

158 The crystal was reacted at three time steps (t_1 to t_3) during 22 h with acidic solutions (pH 4.5 or
 159 pH 4.0) in a mixed-flow reactor ($V = 160$ mL) at room temperature ($25 \pm 2^\circ\text{C}$) and atmospheric
 160 pressure. The inlet solution was prepared with deionized water ($18.2 \text{ M}\Omega\cdot\text{cm}^{-1}$) + 0.01M NaCl
 161 and the pH was adjusted to either 4.5 ± 0.1 or 4.0 ± 0.1 using analytical grade HCl. The flow rate
 162 Q was set to $8 \text{ cm}^3\cdot\text{h}^{-1}$ during the experiment using a Chemyx fusion syringe pump to maintain
 163 far-from-equilibrium conditions, and the solution was stirred at a rate of 400 rpm. The outlet
 164 fluid was collected continuously for analysis of the calcium released with Inductive Coupled
 165 Plasma - Mass Spectroscopy (ICP-MS 7500ce, Agilent Technologies). Internal spikes (In-Re),
 166 blank and calibration standards were used and replicate analyses were performed to assure
 167 accuracy and precision of the chemical analyses. However, because of the low concentration of
 168 Ca at the outlet ($\sim 10^{-6}$ M) and because the inlet solution contains some Ca as trace impurities in
 169 NaCl, it limits the accuracy of the mass balance evaluation.

170 The high fluid-to-mineral volume ratio allows for only a slight increase in the Ca concentration
 171 in the reactor, from $2.0 \cdot 10^{-6}$ to $6.0 \cdot 10^{-6}$ M, corresponding to a saturation state with respect to
 172 calcite of $\Omega < 10^{-9}$ throughout the experiment (calculated with Phreeqc v3.0 using the Phreeqc
 173 database, Parkhurst and Appelo, 2013). The experimental conditions are summarized in Table 1.

174 The reaction extent can be evaluated through the calcite amount removed from the crystal during
 175 the dissolution experiments. The amount of calcite dissolved at any time, $\Delta n_{\text{calcite-chem}}$ (mol), is
 176 given by:

$$177 \quad \Delta n_{\text{calcite-chem}}(t_i) = \int_{t_0}^{t_i} \frac{\delta n_{\text{calcite}}}{\delta t} \delta t = \int_{t_0}^{t_i} F_{Ca} \delta t = \int_{t_0}^{t_i} Q \times \delta(\Delta\text{Ca}) \delta t = \sum_j V_j (\Delta\text{Ca})_j \quad \text{Eq. 1}$$

178 where $\delta n_{\text{calcite}}$ is the change in the amount of calcite (mol), F_{Ca} is the flux of calcium at the
 179 reactor outlet ($\text{mol}\cdot\text{s}^{-1}$), and ΔCa represents the difference between the outlet and inlet calcium
 180 concentrations, i.e., $[\text{Ca}]_{\text{out}} - [\text{Ca}]_{\text{in}}$ ($\text{mol}\cdot\text{m}^{-3}$), j is the number of aqueous samples collected
 181 between t_0 and t_i and V is their volume (m^3).

182 2.3. 3D imaging with X-ray micro-tomography

183 The crystal was imaged before the reaction (t_0) and at the three time steps (t_1 to t_3) over the
184 course of the dissolution experiment using 3D X-ray micro-tomography at the TOMCAT
185 beamline (Stampanoni et al., 2006), Swiss Light Source (Paul Scherer Institute, Switzerland).
186 The crystal was removed from the reactor for imaging in order to avoid any influence of the
187 beam on the experiment (e.g., water radiolysis (Bras and Stanley, 2016; Laanait et al., 2015)).
188 Indeed, in the range $5 < E < 40$ keV, the photons do not possess enough energy to induce atomic
189 displacements directly in crystalline materials (Bras and Stanley, 2016), so that the effects of
190 radiation are non-significant.

191 A total of four data sets were collected during two different data acquisition sessions, with a
192 pixel size of $0.325 \mu\text{m}$, using a $10\times$ magnification diffraction-limited microscope optics. Due to
193 the large height of the crystal compared to the field of view of the sCMOS camera (pco.Edge 5.5,
194 2560×2160 pixels), three vertical scans were taken to image the whole crystal. Each data set is
195 composed of 1701 radiographs collected over a 180° rotation range. Each radiograph was
196 recorded with a monochromatic and parallel beam at the energy of 20 or 21 keV and an exposure
197 time of 200 or 250 ms depending on the data acquisition session. Volume reconstruction was
198 performed from the radiographs corrected from flat field and background noise using an
199 algorithm based on the Fourier transform method (Marone and Stampanoni, 2012).

200 Image processing was achieved with Avizo[®] software. After reconstruction, the different sub-
201 volumes at a given stage were stitched, resulting in volumes of about $1900\times 1250\times 5800$ voxels.
202 Note that due to the large displacement of the vertical stage and recalculation of the rotation axis
203 during reconstruction, a slight mismatch at the junction between the different sub-volumes might
204 be observed. Then, the 3D grayscale volumes were normalized, converted to 8-bit integers, and
205 denoised with a 3D median filter. The crystals were subsequently registered in the same
206 coordinate system using the mutual information-based image registration approach (Maes et al.,
207 1997). The different target volumes were aligned with the reference volume (at t_0), using a tri-
208 linear interpolation technique to recalculate the gray value of the target voxels in the new
209 coordinate system (Gonzales and Woods, 1992). Registration efficiency was evaluated thanks to
210 marks identifiable inside the crystal, like micro-defects or micro-cracks.

211 2.3.1. Evaluation of the crystal volume and surface area.

212 Evaluation of the crystal volume was performed following two different ways. The first method
213 is based on the grayscale histograms of the XMT data sets. The three peaks for air, calcite and
214 glass capillary are clearly identifiable on the histograms (Figure 1), so that a simple threshold
215 value half-way between the peak for air and the peak for calcite is chosen, after removal of the
216 glass capillary peak. The calcite peak area represents the number of calcite voxels, and changes
217 in the peak area of calcite are directly linked to the amount of calcite removed by dissolution.

218 The second method is based on segmentation of the grayscale data sets to provide a discretized
219 geometry of the crystal. However, due to the large size of the data sets (~14 Gb), the volumes
220 were resampled by a factor of two in every direction and interpolated with a Lanczos window
221 function (Meijering et al., 2001) to reduce the volume size by an eight-fold factor before
222 segmentation. The voxel resolution of the resulting volumes is thus 0.65 μm . A region-growing
223 algorithm (Pitas, 2000) was used to separate the whole images into two phases, i.e. air and solid,
224 by selecting, based on their gray-level, a certain amount of voxels which belong with certainty to
225 one of the phases, and incrementally assigning indeterminate voxels to either the solid or the air
226 phase. Although the peaks for air and calcite are well separated on the histograms, this technique
227 is preferred over a simple thresholding method in order to remove the star artifacts present in the
228 air phase, especially at t_0 . Indeed, the star artifacts are very common at the intersection points of
229 angulated elements such as the crystal, pits or macro-steps edges, and they can be confused with
230 solid as they are very bright. After segmentation, the solid objects, i.e., crystal and capillary
231 glass, and the artifacts were labeled in order to separate and remove the capillary glass and the
232 artifacts from the images. The resulting volumes contain only the crystal.

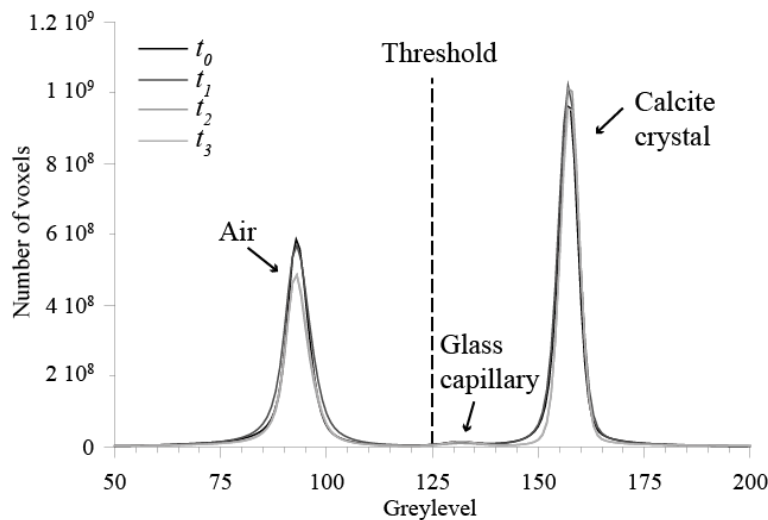
233 The crystal volume $V_{crystal}$ (μm^3) is calculated at t_i from the number of element solid voxels n_{sol} ,
234 i.e., $V_{crystal} = n_{sol} \times V_{voxel}$, with V_{voxel} the volume of a voxel ($0.65 \times 0.65 \times 0.65 \mu\text{m}^3$). The amount of
235 calcite removed, $\Delta n_{calcite-XMT}$, can be evaluated at any stage of dissolution from the XMT
236 volumes according to:

237
$$\Delta n_{calcite-XMT}(t_i) = \int_{t_0}^{t_i} \frac{\delta V_{crystal}}{V_{calcite} \times \delta t} \delta t = \frac{V_{crystal}(t_i) - V_{crystal}(t_0)}{V_{cal}} \quad \text{Eq. 2}$$

238 where v_{cal} is the molar volume of calcite ($\text{m}^3 \cdot \text{mol}^{-1}$).

239 The crystal surface area (μm^2) is calculated at t_i from the number of solid-air pixel interfaces
240 ($n_{sol-air}$), i.e. $S_{crystal} = n_{sol-air} \times S_{pixel}$, with S_{pixel} the surface area of a pixel ($0.65 \times 0.65 \mu\text{m}^2$), which
241 is the smallest element of surface area at the fluid-crystal interface. Note that the whole crystal
242 was considered in the calculations, the surface area of the unreacted part of the crystal
243 representing only about 0.05 % of the surface area of the crystal.

244



245

246 Figure 1. Normalized histograms for the different XMT grayscale data sets. The differences in
247 the peak areas for calcite and air both show the amount of calcite removed by dissolution (i.e., a
248 decrease of the peak area of calcite and, as a result, an increase of the peak area of air).

249

250 2.3.2. Examination of surface topography evolution

251 Surface topography evolution was evaluated locally on some small portions of the crystal faces.
252 A few volumes of interest (VOIs) were extracted on faces 1, 2, and 3, from the grayscale data
253 sets, with the voxel size of $0.325 \mu\text{m}$. The mean planes of the crystal surface extracts were
254 determined at t_0 and registered in a horizontal plane. The transformation was applied to the other
255 VOIs, so that the topography evolution of the surface extracts is directly comparable. This

256 technique is preferred over the extraction of the VOIs from the segmented images, the direct
 257 registration of which, in a horizontal plane, would highlight interpolation steps at the crystal
 258 surface, which can be confused with crystal surface steps (see for instance Figure 2 shown in
 259 Noiriél et al., 2019). After segmentation of the grayscale VOIs using the same procedure as
 260 described above (see section 2.3.1), the topography of the fluid-solid interface was extracted.
 261 When the surface displays some overlaps (as it is the case, for instance, when micro-cracks are
 262 visible inside the crystal), the interface with the lowest surface elevation is selected.

263 2.3.3. Crystal dissolution rate

264 The global crystal dissolution rates r_{diss} (mol·s⁻¹) and rates normalized to the surface area of the
 265 crystal $r_{diss-norm}$ (mol·m⁻²·s⁻¹) were calculated after segmentation of the XMT data sets according
 266 to the following equations, respectively:

$$267 \quad r_{diss} = \frac{\Delta V_{crystal}}{v_{cal} \Delta t} \quad \text{Eq.3}$$

268 and

$$269 \quad r_{diss-norm} = \frac{\Delta V_{crystal}}{\overline{S_{crystal}} v_{cal} \Delta t}, \quad \text{Eq.4}$$

270 with Δt a time interval (s), and $\Delta V_{crystal}$ and $\overline{S_{crystal}}$ the change in crystal volume (m³) and the
 271 average crystal surface area (m²) between two stages of dissolution, respectively.

272 2.3.4. Measure and mapping of the local dissolution rate at the crystal surface

273 Following the methodology described in Noiriél et al., 2019, the local dissolution rate r'_{diss}
 274 (μm·h⁻¹) can be determined at any element (i.e., fluid-crystal pixel interface) of the crystal
 275 surface by analysis of the surface height retreat after each dissolution stage. In their study, the
 276 surface retreat was calculated normal to the closest {10 $\bar{1}$ 4} surface. In the present paper,
 277 however, we have adopted a slightly different method in order to calculate the surface retreat
 278 normal to any element of the crystal surface instead of the retreat normal to the {10 $\bar{1}$ 4} surface.
 279 This methodology is motivated by the fact that: (i) every dissolution stage at t_i (starting from t_1)

280 is compared with the previous one (t_{i-1}), and accounts for the changes of crystal morphology at
 281 the edges and corners at any stage of dissolution, and (ii) the crystal has a morphology far more
 282 complex than a simple rhombohedron. The method permits to measure the dissolution rate at the
 283 crystal surface regardless the crystal geometry or orientation.

284 Practically, the 3D Euclidean distance maps (Akmal Butt and Maragos, 1998; Russ, 2011)
 285 outside of the crystal were computed at any time t_i (for $i=1$ to $i=3$). Consequently, each voxel
 286 outside the crystal at a given time is labeled with the distance normal to its surface, starting from
 287 the position of the fluid-crystal interface. Combining the distance map at t_i with the position of
 288 the fluid-crystal interface at t_{i-1} gives the surface retreat of the crystal normal to the surface of
 289 the crystal at the previous stage of experiment, as illustrated in Figure 2. In this case, for
 290 instance, the surface retreat at the crystal edges (or corners) is the distance normal to the
 291 considered edge (or corner), not the shortest distance (i.e., the distance normal) to the closest
 292 $\{10\bar{1}4\}$ surface.

293 Then, the local dissolution rate normal to the crystal surface is calculated according to:

$$294 \quad r'_{\text{diss}} = \frac{d\mathbf{I}_{\text{fc}} \cdot \mathbf{n}}{dt}, \quad \text{Eq. 5}$$

295 with \mathbf{I}_{fc} the fluid-crystal position vector, and \mathbf{n} the normal to the crystal surface; the product
 296 $\mathbf{I}_{\text{fc}} \cdot \mathbf{n}$ is the surface retreat, i.e., the distance normal to the surface. The rate is expressed as a
 297 retreat velocity at the surface ($\text{nm} \cdot \text{s}^{-1}$ or $\mu\text{m} \cdot \text{h}^{-1}$), but can be averaged at the crystal scale and
 298 normalized to the surface area by (e.g., Arvidson et al., 2004):

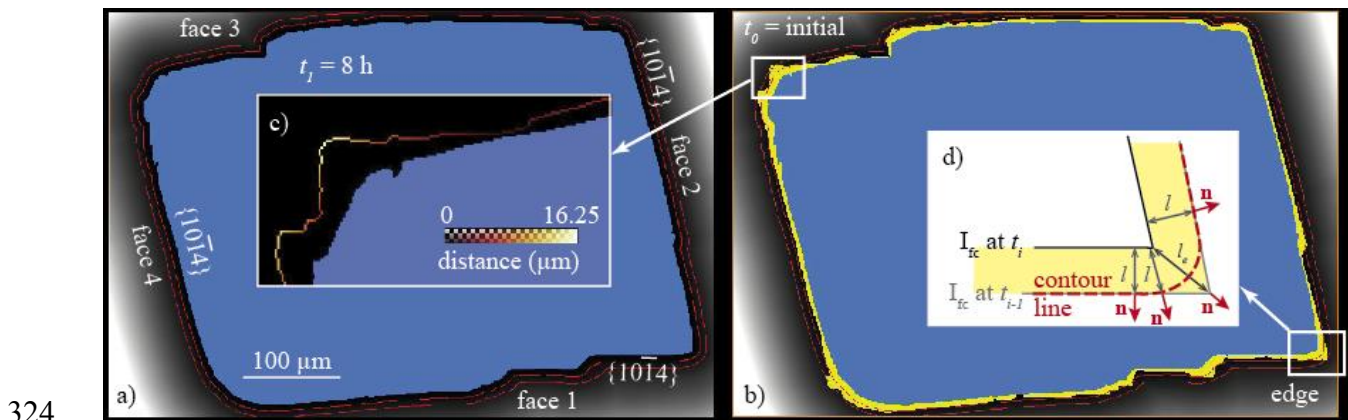
$$299 \quad \bar{r}'_{\text{diss-norm}} = \sum_{n_{\text{sol-fluid}}} \frac{1}{V_{\text{cal}} \times n_{\text{sol-fluid}}} \frac{d\mathbf{I}_{\text{fc}} \cdot \mathbf{n}}{dt}, \quad \text{Eq. 6}$$

300 with $n_{\text{sol-fluid}}$ the number of voxels at the fluid-solid interface. It is also possible to determine the
 301 rate of specific faces, edges or other crystal features by averaging the local dissolution rates from
 302 VOIs defined in these areas:

$$303 \quad \bar{r}'_k = \sum_j \frac{1}{j} \frac{d\mathbf{I}_{\text{fc}} \cdot \mathbf{n}}{dt}, \quad \text{Eq. 7}$$

304 with k being a face, an edge, a corner or another crystal pattern, and j the number of fluid-solid
 305 interface pixels covering its surface. For the faces, VOIs of the same width (i.e, 150 pixels) were
 306 chosen in the central part of the flat portions of the faces (except for face 3) to limit as much as
 307 possible the contribution of edges to the determination of the rates. For the edges, VOIs of the
 308 same section, i.e. 150×150 pixels for the obtuse edges (i.e., edges 4-1 and 2-3, between face 4
 309 and 1, and face 2 and 3, respectively; see Figure 3 for location) and 125×150 pixels for the acute
 310 edges (i.e, edges 1-2 and 3-4) were defined at the same location for the different stages of the
 311 crystal evolution. As the crystal does not exhibit well identified corners, only one VOI around a
 312 large 5-4-1 corner (i.e., at the intersection between faces 5, 4 and 1, see Figure 3 for location)
 313 was selected.

314 The local dissolution rates are computed between the two first experiment stages (i.e., between
 315 t_0 and t_1 , and between t_1 and t_2) and can be directly mapped at the crystal surface, providing an
 316 overview of the dissolution rate distribution. The rates are provided in terms of surface retreat
 317 velocity, so that direct comparison is possible with data derived from AFM or VSI, provided that
 318 the retreat is also measured normal to the surface with these techniques. Appendix A gives
 319 further information about the measurement uncertainty, specifically inherent to the fluid-mineral
 320 positioning and registration issues. Since the number of fluid-crystal interface pixels decreases as
 321 dissolution progresses and the bin width of the histograms decreases with increasing dt , the
 322 dissolution rate distributions are normalized to the distribution at t_2 to allow for a better
 323 visualization.



325 Figure 2. Determination of the surface retreat between two stages of dissolution. (a) 3D distance
326 map (grayscale) outside of the crystal (blue) at t_1 (shown in 2D cross-section), which represents
327 the distance normal to the fluid-solid interface. Distance contours of 10 and 20 pixels (i.e., 6.5
328 and 13 μm) normal to the crystal surface are shown in red. (b) Combining the distance map with
329 the crystal at t_0 (yellow) gives the retreat at the crystal surface between t_0 and t_1 (inset (c)). Inset
330 (d) highlights that, assuming a uniform dissolution of the crystal faces, the distance measured at
331 the edge is actually the normal-distance to the edge, i.e. l_e , not the normal-distance to the surface
332 $\{10\bar{1}4\}$ itself, i.e., $l \cdot \mathbf{n}$ is the normal to the crystal surface at any point belonging to the fluid-
333 crystal interface.

334 2.4. Additional microscopic observations

335 In addition, characterization of the post-reacted sample was conducted using vertical scanning
336 interferometry (VSI) and scanning electron microscopy (SEM) to provide a higher resolution
337 characterization of the crystal surfaces. A Zygo New View 7300 VSI with a 50 \times Mirau objective
338 allowed for mapping surface topographies with a spatial sampling of 0.219 μm along the x and y
339 directions and an effective height resolution of 2-3 nm. The vertical scan range is however,
340 limited to 150 μm , so that observations were restricted to quite flat surfaces. SEM observations
341 were performed with a Jeol JSM-6360LV using the secondary electron mode. These
342 measurements and observations at finer resolution are complementary and will be compared to
343 XMT observations.

344 3. RESULTS

345 3.1. Evolution of the crystal morphology and surface topography

346 The initial crystal morphology, as described in section 2.1, is shown in Figure 3. Dissolution
347 proceeds with heterogeneous face retreat at different scales.

348 At the crystal scale, dissolution of the surface macro asperities such as macro-steps, crystal edges
349 and corners is faster than the average surface retreat (Figure 4), due to the development of
350 numerous steps over the crystal surface. As a result, the flat cleaved surfaces evolve
351 progressively toward curved-shaped surfaces and the crystal becomes rounder with time (Figure

352 4; see also topography profiles in Figure 7). In contrast, dissolution of the topographic lows and
353 at the base of the macro-steps is slower than in the surrounding areas (Figure 4c).

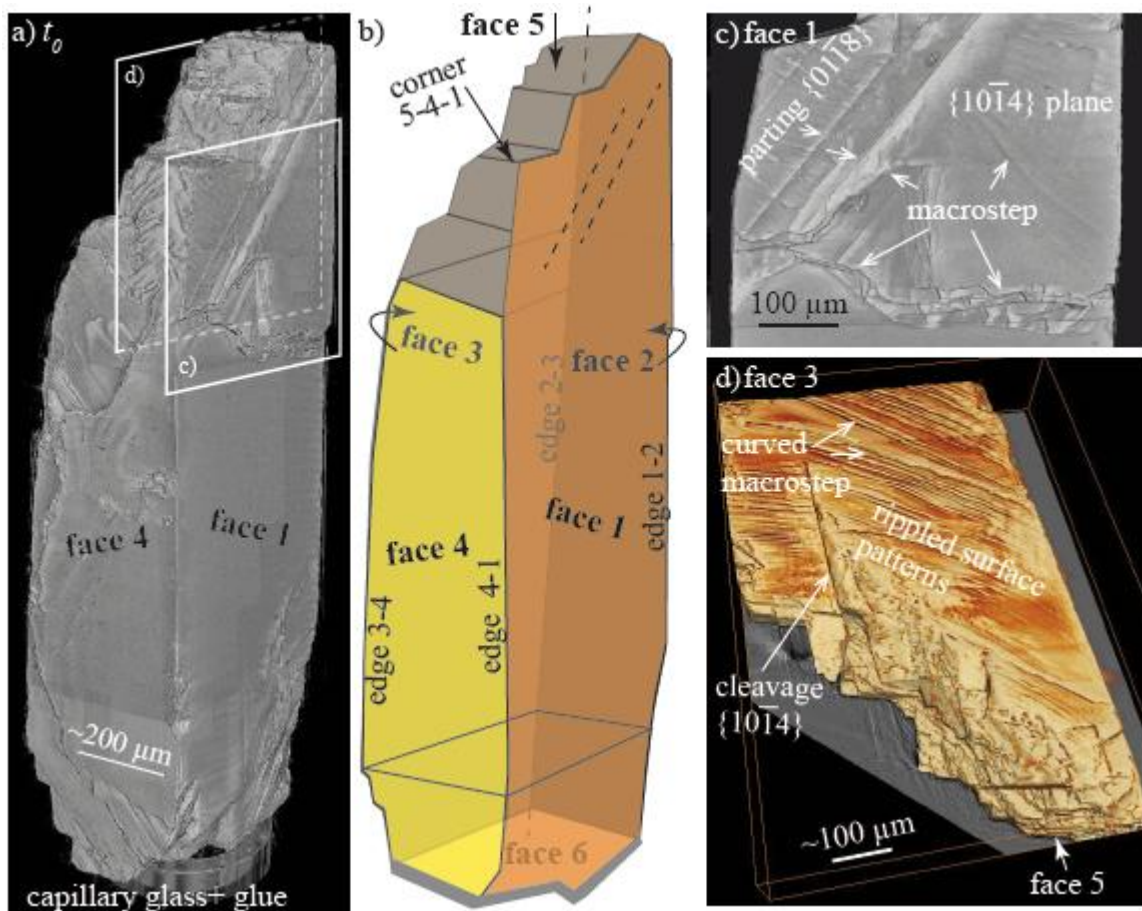
354 At the face scale, the crystal topographies exhibit different evolutions depending on the initial
355 face morphology. At t_1 , the flat faces (i.e. portions of face 1, 2 and 4) are covered by sparse,
356 macro etch pits (Figure 5 and Figure 6), whereas the step-like face (i.e., face 3) does not exhibit
357 any etch pits (Figure 8). The pits certainly result from merging of smaller pits that were formed
358 at the surface at $t < 8$ h, similarly to what has been observed in a comparable experiment at
359 shorter times (Noiriel et al., 2019). The pits are about 90-160 μm in size and 4-7 μm in depth.
360 Their density is variable depending on the face and location, about 100-130 per mm^2 . Several
361 etch pits are likely formed with the assistance of surface micro-defects, i.e., surface scratches, or
362 micro-cracks that can be evidenced inside the crystal (Figure 6a). Their geometry is complex
363 (Figure 6e), and they are generally deeper and remain longer visible than the others. With further
364 reaction (i.e., at t_2 and t_3), the pits of the flat faces tend to annihilate, with a density decreasing
365 to about 40 per mm^2 . This observation confirms the trend in decreasing pit density with
366 increasing dissolution observed in Noiriel et al., 2019. In fact, the development over the surface
367 of numerous steps from the edges progressively annihilate the development of macro-pits, which
368 vanish either by coalescence or by intersecting train of steps coming from the near edge region
369 (Figure 5b,c). Some pits whose dissolution rate becomes at some point slower than the surface
370 average retreat are also evidenced (Figure 5b,c). The anisotropy in step velocities between obtuse
371 and acute steps developed parallel to the crystallographic directions $[\bar{4}41]$ and $[48\bar{1}]$, which
372 results in asymmetrical pit formation, is also visible (Figure 5b and Figure 6b).

373 The evolution of face 3 with a 5° miscut angle is different from the cleaved faces. The surface,
374 which contains a much higher density of steps, does not exhibit any etch pit formation (apart a
375 few small ones along a cleavage continuity (Figure 8)), but the initially curved macro-steps
376 evolve to rippled or serrated steps with potentially rhombohedral endings near the edges (Figure
377 9a).

378 In addition, dissolution is enhanced along straight asymmetric topographic lows corresponding to
379 $\{10\bar{1}4\}$ cleavages (Figure 5 and Figure 8) or $\{01\bar{1}8\}$ parting planes (Figure 9b) that were
380 certainly created during crushing and size reduction of the original crystal. For example, the

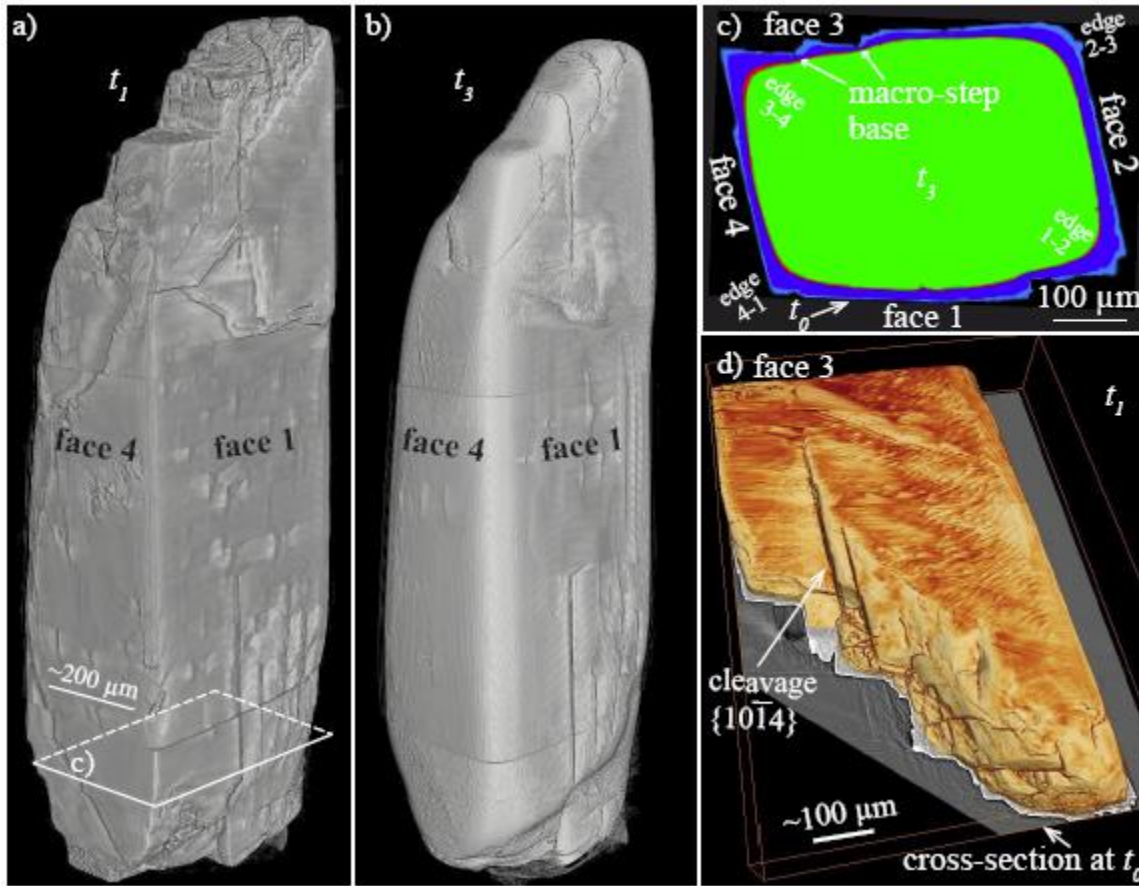
381 $\{10\bar{1}4\}$ cleavage identified at the bottom surface of face 1 reaches about 10 μm in depth from t_2
 382 (Figure 5a and Figure 7a). Dissolution at cleavages is also anisotropic along the $[48\bar{1}]$ direction,
 383 similarly to what is observed at etch pits. Conversely, dissolution at parting planes does not
 384 appear anisotropic. Nevertheless, it generates macrosteps at the crystal surface, probably inherent
 385 to step propagation along these discontinuities (Figure 9b).

386 Finally, the edges are covered with either macrosteps with long straight edges or highly kinked
 387 macrosteps with rhombohedral ending (Figure 9a,c,d). Their morphology actually depends on the
 388 intersection between the calcite dissolution planes with the curved topography of the crystal
 389 (Figure 8 and Figure 9). The patterns have similarities with those observed at finer scale on
 390 misoriented polished surfaces (Bisschop et al., 2006; Smith et al., 2013). However, with further
 391 dissolution, it is worth noting that some flat surface portions reappear near the crystal edges
 392 (Figure 9c,d and Figure 5), often in the continuity of former etch pit propagation direction.



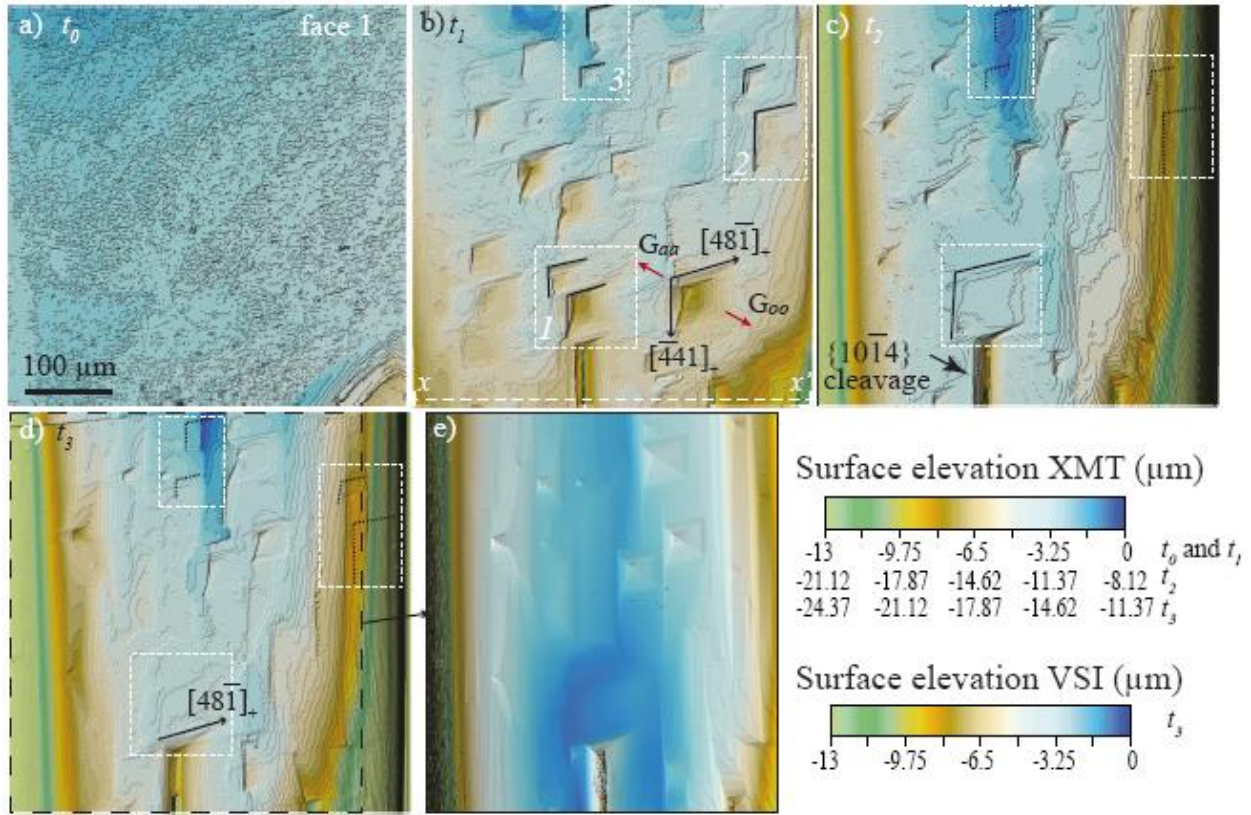
393

394 Figure 3. (a) Volume rendering of the initial calcite crystal obtained from XMT and (b)
 395 schematic representation of the crystal morphology, with numbering of the different faces,
 396 and corner. (c)-(d) Detailed surface patterns: (c) detail from face 1, showing a well cleaved
 397 $\{10\bar{1}4\}$ surface plane with macrosteps; the face is also intersected by several $\{01\bar{1}8\}$ parting
 398 planes, (d) detail from top part of face 3 covered by curved macrosteps and view of the rough
 399 crystal top showing many intersecting $\{10\bar{1}4\}$ planes.



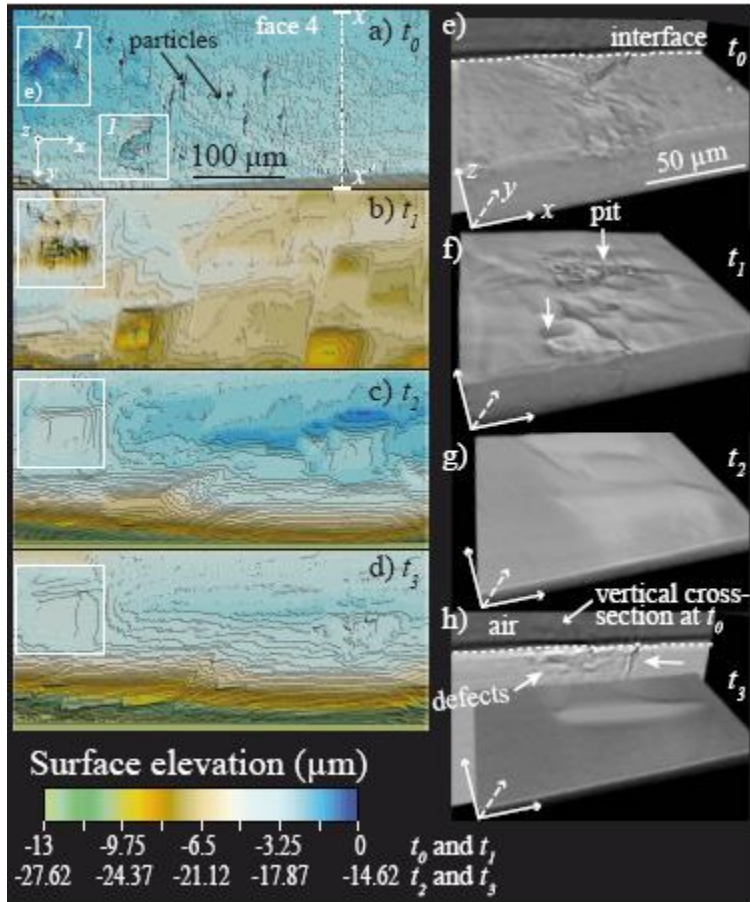
400
 401 Figure 4. Volume rendering of the calcite crystal obtained from XMT at time (a) t_1 and (b) t_3 .
 402 (c) Cross-section of the superimposed segmented volumes from t_0 to t_3 showing heterogeneous
 403 surface retreat and rounding of the edges. The retreat between t_0 and t_1 is shown in light blue,
 404 between t_1 and t_2 in dark blue, and between t_2 and t_3 in red; the crystal at t_3 is in green. (d)
 405 Volume rendering of the top part of face 3 at t_1 .

406



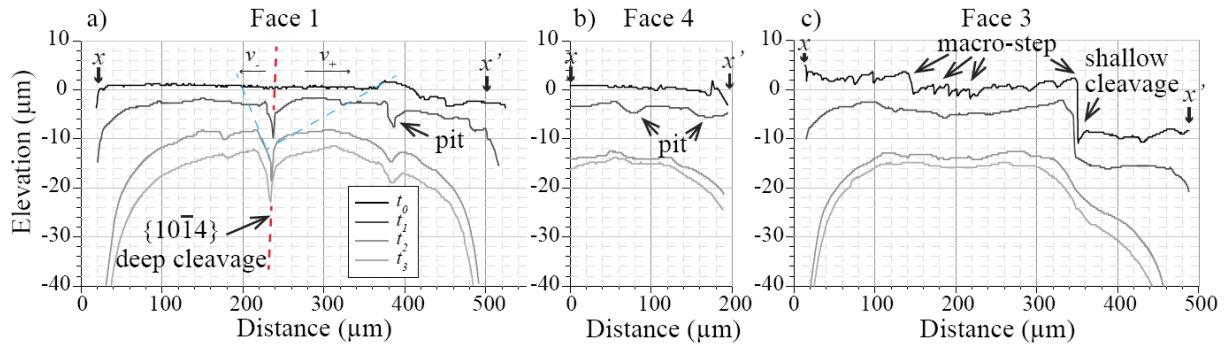
407

408 Figure 5. Evolution of etch pit morphologies at the crystal surface. (a)-(d) XMT-derived
 409 topography for a surface extract of face 1 ($455 \times 455 \mu\text{m}^2$), from t_0 to t_3 . Note that the highest
 410 surface elevation at t_0 was set arbitrarily to 0, and that the range of elevations was shifted by
 411 8.12 and 11.37 μm for t_2 and t_3 , respectively. The figure shows pit annihilation by coalescence
 412 of two pits (inset 1), by intersection with a train of steps (inset 2) or by decrease of its rate of
 413 formation compared to the average surface retreat (inset 3). The black dotted lines correspond to
 414 the reported position of some etch pits at t_1 . The white dotted xx' line in (b) denotes the position
 415 of the topographical profiles shown in Figure 7a. (e) VSI-derived topography at t_3 . Note that the
 416 image is not exactly superimposable with the corresponding XMT image and that the origin for
 417 vertical range is arbitrary.



418

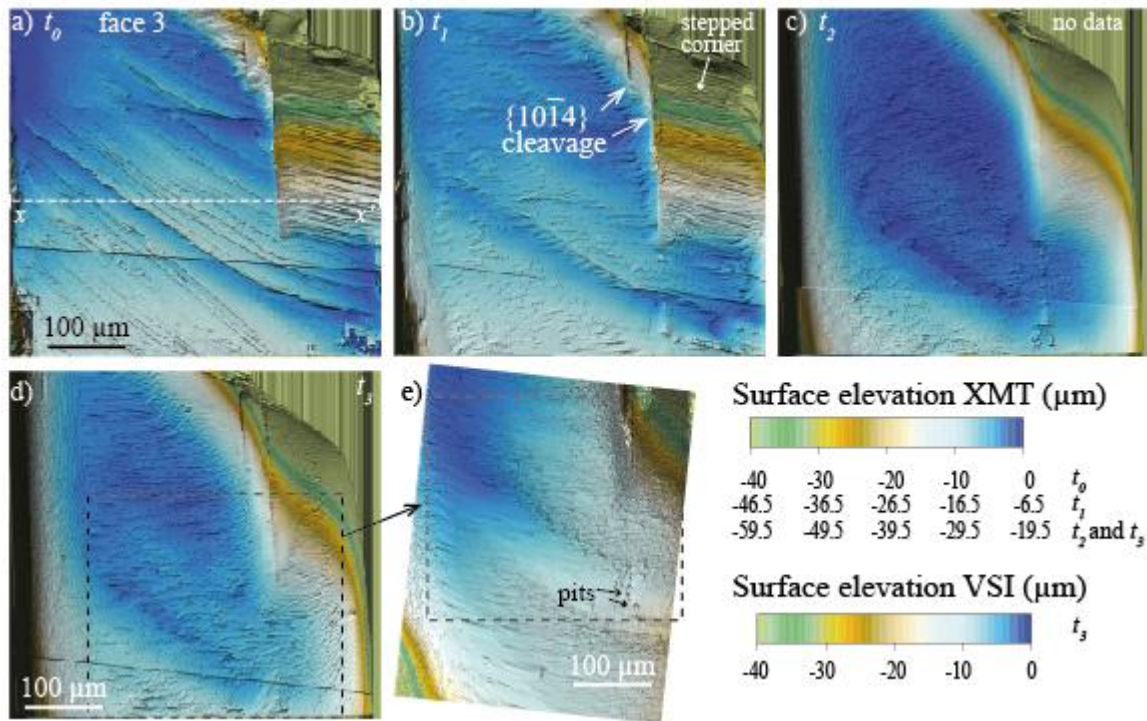
419 Figure 6. Evolution of etch pit morphologies at the surface of face 4 (surface extract of $455 \times$
 420 $195 \mu\text{m}^2$) (a)-(d) XMT-derived topography from t_0 to t_3 . Note that the highest surface elevation
 421 at t_0 and t_1 was set arbitrarily to 0, and that the range of elevations was shifted by $14.62 \mu\text{m}$ for
 422 t_2 and t_3 . (e)-(h) Details of the evolution of a pit geometry (3D rendering view) which initiated
 423 thanks to macro-defects that are visible at the surface (inset 1) and also inside the crystal. Note
 424 that the views are flipped vertically compared to the orientation in (a)-(d). The vertical white
 425 dotted xx' line in (a) denotes the position of the topographical profiles shown in Figure 7b.



426

427 Figure 7. Topography evolution (xx' profiles) of (a) face 1 (b) face 4 and (c) face 3 at the
 428 different times of the experiment (see Figure 5, Figure 6 and Figure 8 for the localization of the
 429 profiles). The red dashed line underlines the position of the $\{10\bar{1}4\}$ cleavage direction. The blue
 430 dashed lines underline the direction of the $[48\bar{1}]_+$ and $[48\bar{1}]_-$ facets at t_2 .

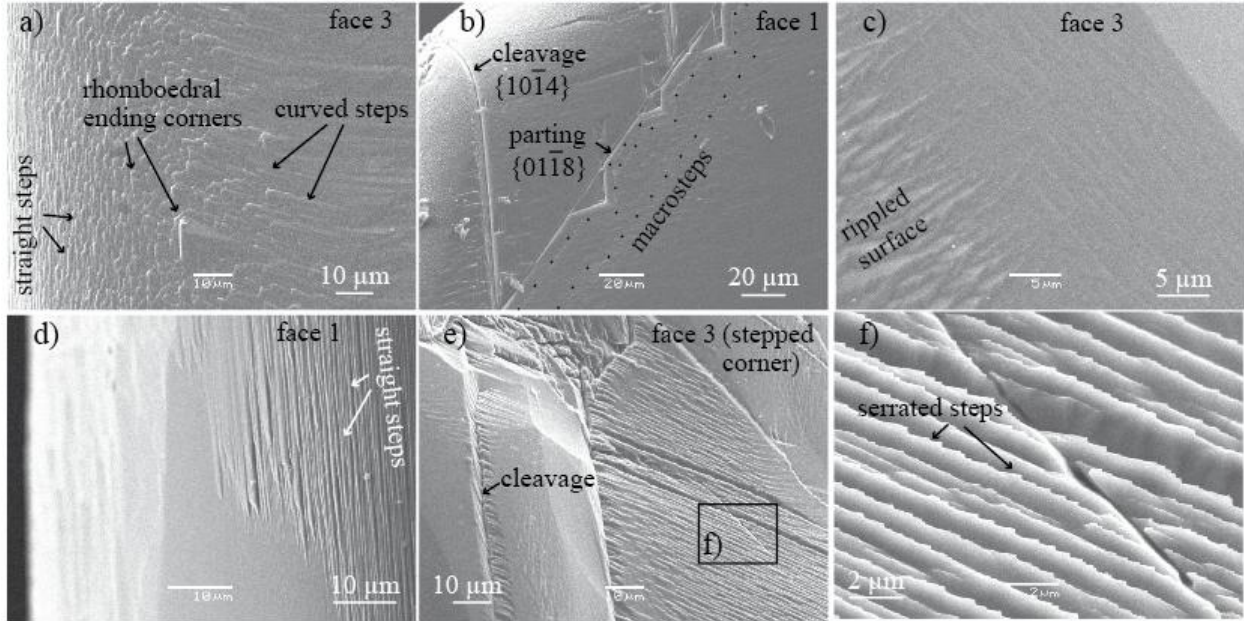
431



432

433 Figure 8. Evolution of the surface morphology of face 3. (a)-(d) XMT-derived topography from
 434 t_0 to t_3 (surface extract of $487 \times 487 \mu\text{m}^2$). Note that the highest surface elevation at t_0 was set
 435 arbitrarily to 0, and that the range of elevations was shifted by $6.5 \mu\text{m}$ for t_1 , and by $19.5 \mu\text{m}$ for

436 t_2 and t_3 . (e) VSI-derived topography at t_3 . Note that the image is not superimposable with the
 437 corresponding XMT image and that the origin for vertical range is arbitrary. The horizontal
 438 dotted xx' line denotes the position of the topographical profiles shown in Figure 7c.



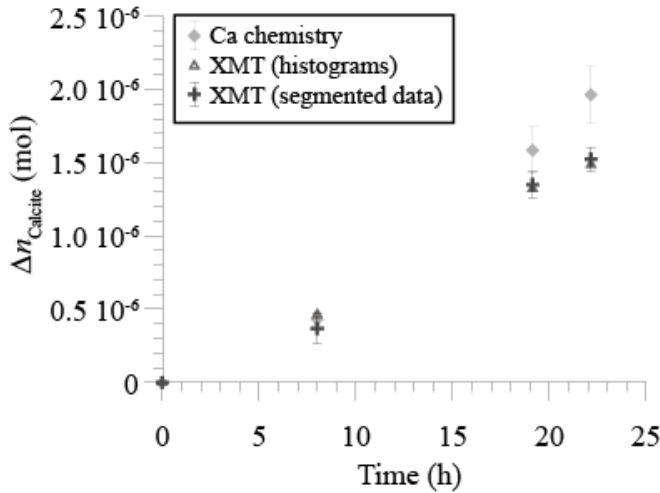
439
 440 Figure 9. SEM observations of the calcite crystal at t_3 . (a) Rhombohedral ending corners at the
 441 junction between straight steps and curved steps at the crystal edge 2-3. (b) Anisotropic
 442 dissolution across a $\{10\bar{1}4\}$ cleavage and dissolution across a $\{01\bar{1}8\}$ parting plane intersecting
 443 several $\{10\bar{1}4\}$ cleavages; the black dots underline macrosteps propagating at the crystal surface
 444 from the parting plane. (c) Transition between rippled steps and flat surface portion at the crystal
 445 edge 3-4. (d) Transition between straight steps and flat surface portion at the crystal edge 1-2. (e)
 446 Highly cleaved and fractured area near cleavages (stepped corner of face 3, see Figure 8 for
 447 location) exhibiting (f) serrated steps.

448

449 3.2. Global dissolution rate and surface rate distributions

450 The experimental calcite crystal dissolution takes place under far-from-equilibrium conditions,
 451 with the saturation state Ω ($\Omega = IAP / K_{s\text{ calcite}}$) remaining below 10^{-9} . The amount of dissolved
 452 calcite derived from XMT and chemical balance is depicted in Figure 10. First, the figure shows

453 that the amount of calcite derived from the XMT processing techniques, i.e. the (i) grayscale
 454 histograms and (ii) segmented data sets, are in very good agreement. However, at t_2 and t_3 , the
 455 results are slightly lower than $\Delta n_{\text{calcite-chem}}$ derived from chemical analyses.



456

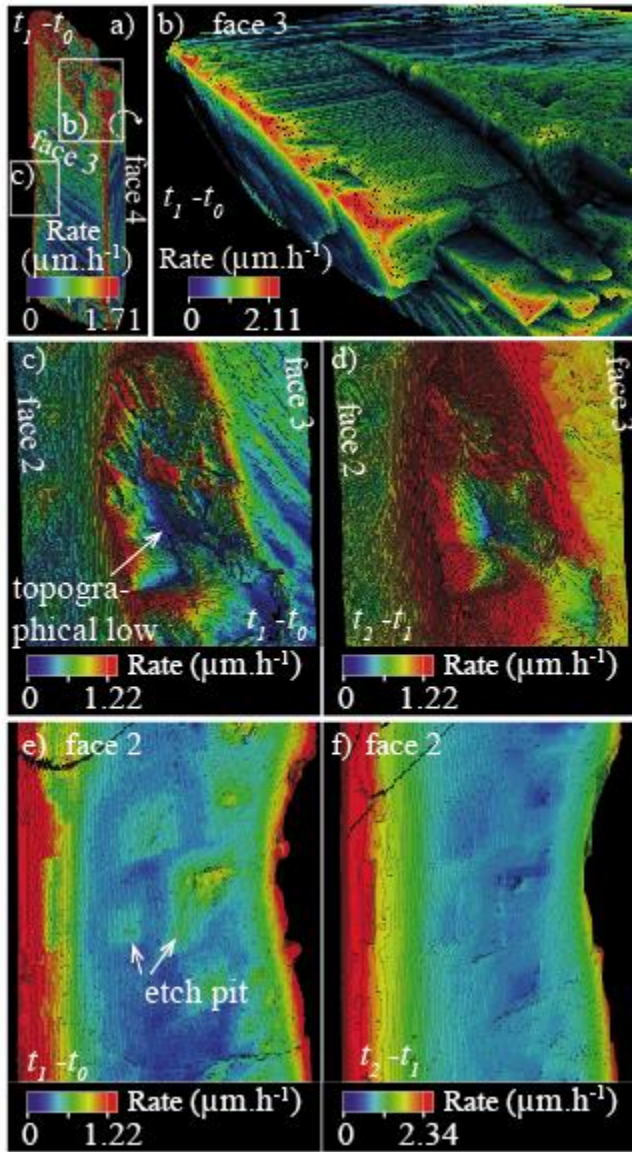
457 Figure 10. Amount of calcite dissolved during the experiment, calculated from XMT grayscale
 458 or segmented data sets ($\Delta n_{\text{calcite-XMT}}$) and from Ca chemical balance ($\Delta n_{\text{calcite-chem}}$). The error bar
 459 on the data derived from XMT segmented data set is calculated assuming an error of ± 1 pixel
 460 (i.e., $0.65 \mu\text{m}$) on the position of the fluid-crystal interface.

461

462 Analysis of the XMT segmented data shows that both the crystal volume and surface area
 463 decrease during dissolution (Table 2). At the end of the experiment, 21.4% of the crystal was
 464 dissolved. The global dissolution rates, r_{diss} , as well as the average surface normalized rates,
 465 $r_{\text{diss-norm}}$, are also presented in Table 2. In this study, the global rate was normalized to the
 466 surface area determined at the scale of the XMT imaging technique. The specific surface area of
 467 the unreacted crystal determined this way is $43.9 \text{ cm}^2 \cdot \text{g}^{-1}$, which is 2.7 times smaller than the
 468 surface area determined by BET (Brunauer et al., 1938) on similar calcite crystals ($120 \text{ cm}^2 \cdot \text{g}^{-1}$,
 469 Noiriél et al., 2012). As expected, the global rate is higher at pH 4.0 ($9.25 \times 10^{-6} \text{ mol} \cdot \text{m}^{-2} \cdot \text{s}^{-1}$) than
 470 at pH 4.5 ($5.46 \times 10^{-6} \pm 1.21 \times 10^{-6} \text{ mol} \cdot \text{m}^{-2} \cdot \text{s}^{-1}$). The rate determined at pH 4.0 is in good
 471 agreement with the data obtained by Noiriél et al., 2019 using the same technique and at the

472 same pH value. The rate determined at pH 4.5 seems to increase with increasing dissolution time,
473 but it is difficult to decipher whether it results from the crystal geometry changes or from the
474 preceding dissolution stage at pH 4.0 (i.e., between t_1 and t_2).

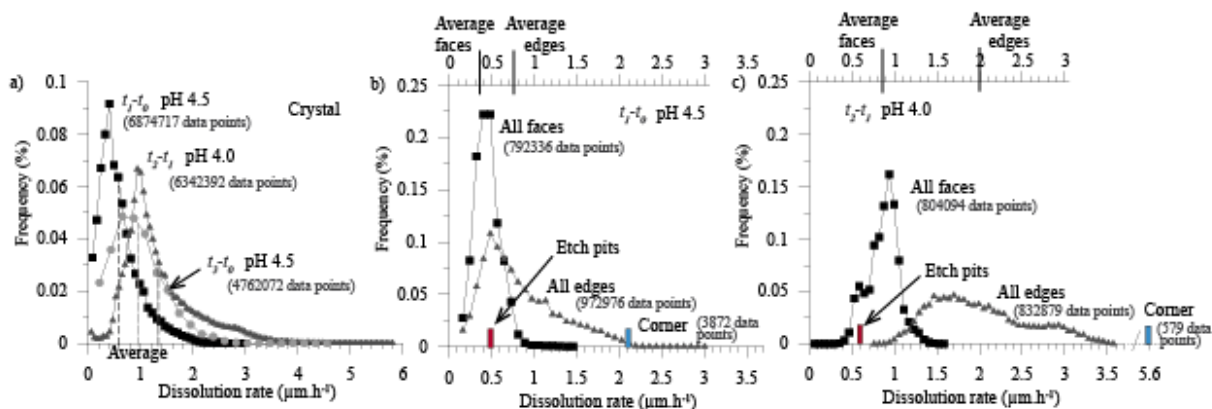
475 More interesting is the evaluation of the local dissolution rates directly mapped at the crystal
476 surface (Figure 11), as well as the derived rate distributions (Figure 12). The local dissolution
477 rates at the crystal surface reaches on average 0.59 (between t_0 and t_1), 1.34 (between t_1 to t_2),
478 and $0.94 \mu\text{m}\cdot\text{h}^{-1}$ (between t_2 to t_3) (Table 2). The average local normalized rates, $\bar{r}'_{diss-norm}$, differ
479 slightly from the average global rates, $\bar{r}_{diss-norm}$, which are in turn normalized to the total crystal
480 surface area (Table 2). Mapping of the dissolution rates confirm the observations made from the
481 surface retreat. The average dissolution rate results from the contribution of the different crystal
482 surface patterns to dissolution at very different rates. The reactivity extracted from small VOIs at
483 the crystal corner (\bar{r}'_{corner}) and edges (\bar{r}'_{edge}) appears to be the fastest process, followed by the
484 reactivity of the cleavage micro-fractures and parting planes ($\bar{r}'_{cleavage}$), macrosteps ($\bar{r}'_{macrostep}$) and
485 etch pits (\bar{r}'_{pit}), faces, and finally topographic lows and base of macrosteps ($\bar{r}'_{macrostep\ base}$) (Figure
486 11 and Figure 12b,c).



487

488 Figure 11. Mapping of the local dissolution rate \bar{r}'_{diss} ($\mu\text{m}\cdot\text{h}^{-1}$) at the crystal surface. (a) Mapping
 489 of the whole crystal between t_0 and t_1 , showing higher rates at the crystal edges and corners. (b)
 490 Detail of the stepped corner in face 3. (c)-(d) Detail of the topographic low at the edge 2-3 at (c)
 491 pH 4.5 (i.e., between t_0 and t_1) and (d) pH 4.0 (i.e., between t_1 and t_2). (e)-(f) Detail of the
 492 local rates at the surface of face 2 at (e) pH 4.5 (i.e., between t_0 and t_1) and (f) pH 4.0 (i.e.,
 493 between t_1 and t_2). Note that values in red exceed the maximum values indicated in the scale
 494 bars.

495



496

497 Figure 12. (a) Local rate distribution at the surface of the whole crystal. The rates are normalized
 498 to the distribution at t_2 for the sake of visualization. (b)-(c) Averaged rates determined for the
 499 four faces and edges (extracted from 8 different VOIs), and for the corner (extracted from 1
 500 VOI) at (b) pH 4.5 (i.e., between t_0 and t_1) and (c) pH 4.0 (i.e., between t_1 and t_2). The rates
 501 evaluated for the etch pits shown in Figure 11e,d are also presented. The number of data points
 502 in the VOIs used for the calculation of the histograms is also indicated.

503

504 4. DISCUSSION

505 4.1. Application of X-ray micro-tomography for tracking crystal reactivity

506 XMT is a noninvasive and nondestructive imaging technique relying on the 3D reconstruction of
 507 a sample from a series of 2D radiographic projections taken at about a thousand of different
 508 angular positions over 180° . The development of fast detection systems, high-quality optics, high
 509 data rate streaming and computational capabilities has resulted in new perspectives for the
 510 application of XMT imaging (Marone and Stampanoni, 2012; Villanova et al., 2017), such as *in*
 511 *situ* dynamic tracking of fast reactions with a micrometric resolution, or *ex situ* imaging with a
 512 submicrometric resolution (i.e., with a pixel size up to about 50 nm) at well-spaced intervals, like
 513 in this study.

514 Admittedly, XMT has a lower resolution than VSI, especially in the direction perpendicular to
 515 the surface. For instance, XMT and VSI maps reported in Figure 5d,e and Figure 8d,e show that

516 the finest details are not resolved, like the pit topography or some surface details. However, there
517 is a high degree of consistency between the methods, and all the etch pits observed with VSI are
518 identifiable with XMT. XMT reveals also a good match with SEM observations in areas where
519 VSI is unable to capture the surface elevation due to steep topographical changes (Appendix B).

520 Comparison of VSI and XMT techniques for five different profiles at the surface of face 1
521 (Figure A.1 in Appendix A) shows that XMT effectively may misestimate the position of the
522 fluid-mineral interface, especially at high elevations. An uncertainty estimate of ± 1 pixel seems
523 nonetheless reasonable when comparing the different profiles. The inability of XMT to capture
524 some surface details does not arise only from the imaging resolution, and some inherent noise
525 can also alter the images. Indeed, XMT does not provide a direct measurement of the surface
526 topography. Conversely, the topography is extracted from the 3D reconstructed grayscale
527 volumes of the crystal after segmentation. This makes the accuracy on the fluid-mineral
528 positioning dependent on the grayscale image quality. In particular, the star artifacts, which are
529 noticed over the crystal surface (especially in the data set at t_0), manifest themselves as bright or
530 dark streaks where angular shapes exist, like at the crystal edges, in micro-cracks and etch pits.
531 Consequently, they can introduce a bias locally on the topography extracted by altering image
532 segmentation (see, for instance, the vertical depressed area around the particles in Figure 6a). In
533 particular, they were identified to be the cause of the topography alteration near the high
534 elevation patterns.

535 Nevertheless, the technique has advantages over other surface-sensitive methods, as there is no
536 restriction on the crystal orientation or geometry, especially in terms of face orientation or
537 surface roughness, so that any type of crystal or surface morphology can be analyzed. No
538 specific preparation that can affect mineral reactivity (e.g., polishing or crushing) is required, and
539 the whole crystal geometry is provided, accounting for the reactivity of all the faces, edges and
540 corners. In addition, experiments are not restricted to small surface retreat due to unlimited
541 vertical range, so that exploration of reactivity on the long term is possible. The technique also
542 allows for recalculating the changes in the geometric surface area with time, something useful
543 for the conventional rate normalization. Finally, XMT can provide extra information about
544 defects that are located below the surface, i.e., inside the crystal, such as micro-cracks,

545 cleavages, fluid or mineral inclusions, which can contribute at some point to the reactivity, but
546 are hidden from the view of other techniques measuring the topography.

547 Then, the reliability of the method to provide accurate rate distributions from experiments
548 performed *ex situ* relies on the ability to perfectly reference the sample in the same coordinate
549 system, as the crystal has to be moved in and out of the beamline between acquisitions and
550 dissolution experiments. In this case, registration problems can also affect the accuracy of the
551 surface retreat determination (Figure A.2 in Appendix A). In the present study, for instance,
552 clipping of the crystal in three sub-volumes which exhibit a small mismatch and rotation axis tilt
553 did not make registration of the crystal perfectly accurate. When the retreat is too small
554 compared to the pixel size (e.g., between t_2 and t_3), it increases the relative error on the retreat
555 determination. However, this problem of registration could be easily overcome in the future by
556 limiting imaging of the whole crystal to one data set, thus decreasing the pixel size for the crystal
557 to fit in the field of view of the camera, or by creating some masked areas at the crystal surface
558 to facilitate 3D registration of the different data sets.

559 4.2. Contribution of the crystal edges and corners

560 Dissolution at edges and corners increases the population of step and kink sites over time
561 (Arvidson et al., 2003; Briese et al., 2017; Chen et al., 2014; Lüttge et al., 2013), consistently
562 with larger dissolution rates measured at the crystal edges and corners. During dissolution of
563 calcite at pH 4.0, Noiriel et al., 2019 estimated the dissolution rate of the crystal edges to be 1.7
564 times higher than the faces. The results are consistent with this study, where the rate was found
565 to be 2.0 (pH 4.5) and 2.1 times (pH 4.0) higher in average at the crystal edges (Figure 12b,c).
566 The only difficulty in quantifying the contribution of the crystal edges is that their limits become
567 undefined from t_0 , i.e. from the time that the sharp edges evolve to rounded ones, so that the rate
568 distribution at the edges depends on their extension in the VOIs used for calculation.

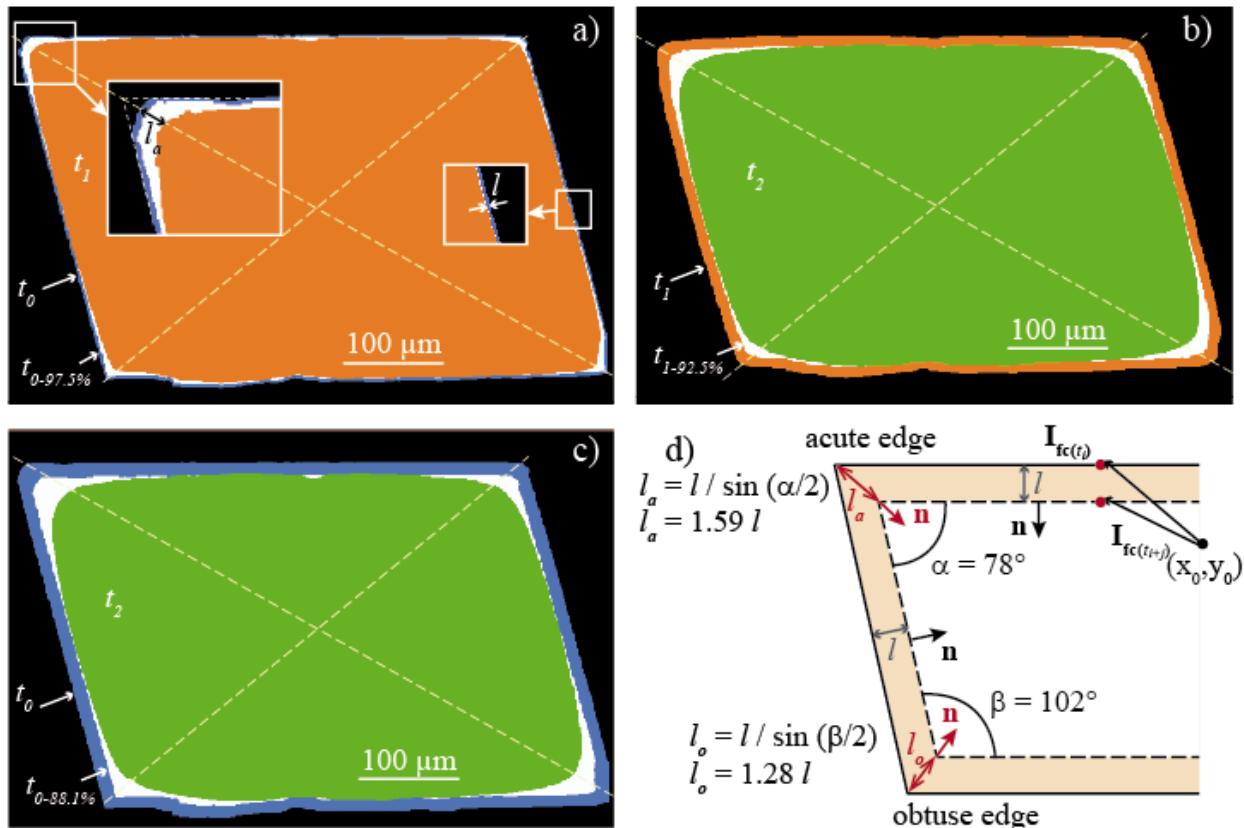
569 Although the edge regions are likely to be dominated by macro-steps, i.e., merged steps formed
570 by step bunching, step pinning and step-step interactions (Bonzel, 2003; Smith et al., 2013),
571 whose velocity is decreased compared to monolayer steps (Akutsu, 2014), it does not limit the
572 lateral extension of the vicinal r-plane edge surfaces from the edges, as suggested by the rounded
573 topographical profiles (Figure 7). By extending the asymmetrical facets of the cleavage in the

574 $[48\bar{1}]_+$ and $[48\bar{1}]_-$ directions up to the initial surface (red and blue dashed lines in Figure 7a),
575 we estimate obtuse (v_+) and acute (v_-) step velocities of 1.5 and 0.64 $\text{nm}\cdot\text{s}^{-1}$ between t_0 and t_2
576 (Figure 7a), two values lower but in reasonable agreement with the velocities obtained at pH 4.3
577 by De Giudici, 2002 (i.e., 4.3 and 1.1 $\text{nm}\cdot\text{s}^{-1}$ for steps oriented along the two equivalent
578 directions $[\bar{4}41]_+$ and $[48\bar{1}]_+$, and $[\bar{4}41]_-$ and $[48\bar{1}]_-$, respectively). These values are largely
579 higher than the face-specific (i.e., normal to the surface) average retreat velocities of 0.1 (pH 4.5)
580 and 0.24 $\text{nm}\cdot\text{s}^{-1}$ (pH 4.0) (Figure 12b,c), that could be assumed to result, in first approximation,
581 of the layer-by-layer stripping during stepwave propagation. Compared to the average retreat
582 velocities of 0.21 (pH 4.5) and 0.55 $\text{nm}\cdot\text{s}^{-1}$ (pH 4.0) determined at the crystal edges, this also
583 supports the assumption that the step density coming from the edges is higher than those coming
584 from the flat surface. Consequently, contribution of the crystal edges to dissolution through the
585 propagation of high velocity trains of steps overrides progressively the effects of the dissolution
586 normal to the $\{10\bar{1}4\}$ faces through pit formation and growth (i.e., the face-specific dissolution).

587 This finding compares also well with a macroscopic comparison model between the
588 experimental dissolution of the crystal (hereinafter referred to as the experiment) and a
589 hypothetical, uniform dissolution of the crystal faces (hereinafter referred to as the uniform
590 dissolution case). Uniform dissolution of 2.5% (from the crystal geometry at t_0) and 7.9% (from
591 the crystal geometry at t_1) in volume of the crystal faces allows for the faces of the scaled crystal
592 to fit in the faces of the real crystal at t_1 and t_2 , respectively (Figure 13a,b). Based on the
593 volume ratios of the crystal in the experiment over the uniform case, accounting for the
594 contribution of the edges shows that the dissolution rate in the experiment is roughly 2.1 time
595 faster between t_0 and t_1 , and 1.5 time faster between t_1 and t_2 compared to what would be a
596 face-specific contribution in the uniform dissolution case. Overall, between t_0 and t_2 , the
597 dissolution rate is 1.6 time higher in the experiment compared to the uniform dissolution case.
598 These results are consistent with the edge-to-surface retreat ratios, as defined by: l_a/l and l_o/l
599 for acute or obtuse edges (with l the retreat normal the face surface, and l_a and l_o the retreat
600 normal to the acute and obtuse edges, respectively). The ratios l_a/l and l_o/l are equal to 1.59
601 and 1.28, respectively, for a uniform dissolution of a parallelogram, as illustrated in Figure 13d.
602 Calculating the ratios from the XMT data show that the dissolution along the edge bisectors is

603 overall 2.4 time faster in the experiment compared to the uniform dissolution case. Rounding of
 604 the crystal edges is thought to decrease the edge to surface retreat ratio with increasing
 605 dissolution, although it is still visible at t_3 (pH 4.5) that the edges have a higher surface retreat
 606 than the faces (Figure 4c).

607 Finally, it is also possible that the crystal edges experience a higher diffusive flux at their surface
 608 in relationship with local hydrodynamic conditions, as dissolution of calcite is diffusion-limited
 609 far from equilibrium under acidic pH (Plummer et al., 1978; Rickard and Sjöberg, 1983), with
 610 the result of enhancing their progressive control to crystal dissolution. Nevertheless, Saldi et al.,
 611 2017 suggested that the reactivity of edges and corners is not limited to low pH and far-from-
 612 equilibrium conditions, and should also be considered carefully at basic pH and near equilibrium
 613 conditions, as the edges can also be the main source of steps moving while etch pit nucleation at
 614 point defects and dislocation would be comparatively unfavorable in these conditions.



615
 616 Figure 13. Superimposed cross-sections of the crystal (a) at t_0 (blue) and t_1 (orange), (b) t_1 and
 617 t_2 (green), and (c) t_0 and t_2 , and comparison with a hypothetical, uniform dissolution of the

618 crystal faces of 2.5% (a), 9.7% (b) and 11.9% (c) in volume (white). Inset 1 shows that the edges
619 are not necessarily sharp, even at t_0 . The white area corresponds to the difference of volume of
620 material removed between the experimental data and the model of uniform dissolution of the
621 crystal faces (i.e., ignoring the edge contribution). (d) Sketch comparing the surface retreat
622 normal to the $\{10\bar{1}4\}$ faces (l) and at the acute (l_a) and obtuse (l_o) edges for a uniform
623 dissolution of the crystal faces; \mathbf{n} is the normal to the surface.

624

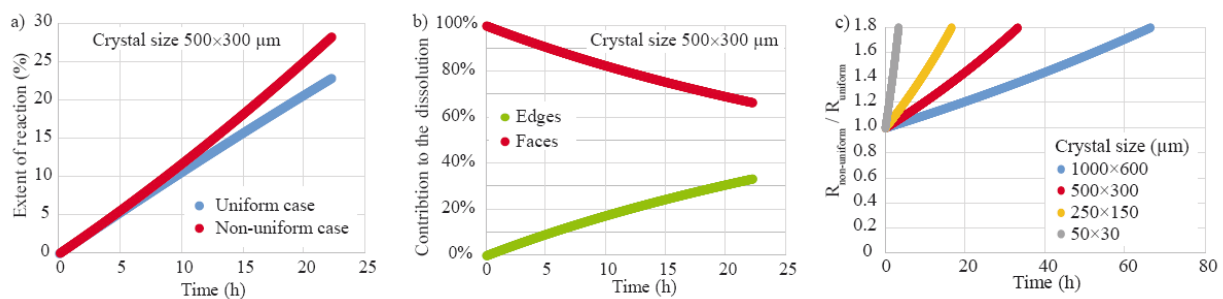
625 4.3. Size- and time-dependent reactivity model

626 The rate data determined in this study are characteristic of the present crystal (i.e., with a given
627 size and aspect ratio), but, all in all, these observations point out that the edge to face-specific
628 contribution will be size-dependent. To the first order, the respective contribution of edges and
629 faces to crystal dissolution can be modeled using simple geometric considerations that are
630 detailed in Appendix C. To emphasize the role of the crystal edges, an ideal case of uniform
631 dissolution of the faces, similar to the actual sketch represented in Figure 13d was compared to a
632 dissolution case including extra contribution of the edges to the dissolution flux (hereinafter
633 referred to as the non-uniform dissolution case). The contribution of the edges to the dissolution
634 flux was approximated to that of the development of facets with an orientation normal to the
635 bisectors of the four angles that define an ideal parallelogram. Importantly, our approach is not
636 mechanistic but geometric; as a consequence, it provides a lower bound for the actual
637 contribution of edges, since the lateral propagation of steps from the edges on the surface is
638 ignored.

639 The evolution of the expected extent of reaction of a model crystal with dimensions similar to the
640 one used in the present study ($500 \times 300 \mu\text{m}$) with no extra contribution of the edges (uniform
641 dissolution case) is compared to that of a crystal with preferential dissolution occurring at the
642 edges (non-uniform dissolution case) (Figure 14a,b). The rate parameters were derived from the
643 dataset discussed in the previous section. As can be seen, the contribution of edges is responsible
644 for a deviation from the sub-linear trend depicted by the trend observed for the uniform case
645 (Figure 14a). After 22.1 hours (corresponding to the duration of the experiment), the extent of
646 reaction is 25% greater because of the contribution of edges, whose dissolution is roughly

647 responsible for one third of the dissolution flux (Figure 14b). This contribution is anticipated to
648 become increasingly significant as the dissolution proceeds and the crystal shrinks.

649 As a consequence, an important concern is how these results obtained with a crystal having the
650 dimensions of the one used in the present study translates to crystals with other grain sizes
651 typical of those used in powder dissolution experiments. To address this question, sensitivity
652 tests were performed and are depicted in Figure 14c, which represents the evolution of the ratio
653 of the non-uniform (i.e., where the reactivity of edges is considered to be similar to that
654 measured in the present study) over uniform (i.e., where the reactivity of edges is dictated by the
655 inwards progression of faces) calcite dissolution rate as a function of time. A ratio greater than 1
656 corresponds to a dissolution rate that is gradually driven by edges, whereas a value of 1 indicates
657 that the contribution of edges is not significant, and that the classical normalization of the rates to
658 the surface area may remains valid. As can be expected, the contribution of edges increases when
659 the grain size decreases (Figure 14c). Over durations as short as ~ 3 days, the enhanced
660 dissolution at edges is responsible for doubling the dissolution flux for crystals with arbitrary
661 dimensions of $50 \times 30 \mu\text{m}$. The time required to reach such a value is obviously much longer as
662 the crystal size increases, and can be as high as ~ 2 months for crystals in the mm-size range.
663 These results illustrate how sensitive is the dissolution of calcite crystals to the crystal size, an
664 effect which must be taken into account when running powder dissolution experiments, and
665 which is less significant for, for instance, VSI experiments conducted with cm-sized crystals.
666 These results also challenge the proper definition of a unique and time-invariant “dissolution rate
667 constant” for crystals, as previously emphasized by Pollet-Villard et al., 2016a or Briese et al.,
668 2017, with similar arguments.



669
670 Figure 14. (a-b) Outputs of the geometric model of calcite dissolution, for a $500 \times 300 \mu\text{m}$ crystal
671 size similar to the one investigated by XMT. (a) Evolution of the extent of reaction for uniform

672 dissolution compared to non-uniform dissolution, where the enhanced dissolution at edges is
673 accounted for. (b) Modeled contribution of edges and faces to the dissolution rate of calcite for
674 the non-uniform case. (c) Modeled non-uniform over uniform ratio of calcite dissolution rates for
675 various crystal sizes. See Appendix C for details of the calculations.

676 4.4. Contribution of the misoriented face and crystal defects.

677 In this study, it is difficult to evaluate precisely the contribution of the misoriented face (i.e., face
678 3) due to registration issues, although it seems that the dissolution rate is higher for face 3 than
679 for face 1 and that the discrepancy is even more pronounced with increasing dissolution.
680 Nonetheless, face 3 clearly experiences a higher heterogeneity in rate distribution, due to the
681 presence of macrosteps whose dissolution is enhanced at their top and reduced at their base. It is
682 expected that the surface with higher energy will evolve to lower energy configuration (Smith et
683 al., 2013). At the end of the experiment, the surface remains covered with rippled steps, except at
684 some locations near the crystal edges (Figure 9c), indicating that this low energy configuration
685 has not been reached yet, despite an average surface retreat of about 22 μm .

686 Crystal defects that were created during the initial crystal crushing and size reduction also
687 contribute to dissolution by increasing locally the dissolution rates. The dissolution rate along
688 cleavages is clearly enhanced (Figure 9c), anisotropic along the $[48\bar{1}]$ direction, and also might
689 be limited by diffusion. This latter statement is supported by the observation that the depth of the
690 deep cleavage shown in Figure 7a does not increase between t_2 and t_3 . In contrast, we can
691 clearly see that the topography is affected in the vicinity of the cleavage, expanding the area of
692 influence of the cleavage along the $[48\bar{1}]_+$ and $[48\bar{1}]_-$ directions, similarly to what can be
693 observed at a smaller scale in etch pits, and at a larger scale at crystal edges. This is also visible
694 for parting planes (Figure 9b), although dissolution at parting plane is not anisotropic like at
695 cleavages. However, discontinuities at their surface serve as well for trains of steps to initiate and
696 propagate over the surface. These observations clearly show how sample preparation can infer on
697 determination of the reaction rates, and that finely crushed crystals will experience higher
698 dissolution rates due to a higher number of defects at the crystal surface and inside that favor
699 step propagation over the crystal surface.

700 Comparison of local rates on cleaved faces interestingly shows that rates at etch pits are initially
701 (i.e., between t_0 and t_1) faster than the average surface retreat (Figure 11e). However, the trend
702 is reversed afterwards (Figure 11f). Noiriél et al., 2019 also observed the progressive
703 disappearance of etch pits at constant pH 4.0 while their rate of formation was initially higher
704 than the average face retreat, similarly to this study. The main assumption to explain this
705 phenomenon arises from the increasing contribution of steps coming from the edges that take
706 over the surface retreat by etch pit growth or spontaneous pit formation at the $\{10\bar{1}4\}$ surfaces.
707 This is supported by the fact that the closer the etch pits to a crystal edge, the faster they
708 disappear. However, dissolution in etch pits might also be limited by diffusion (Bouissonnié et
709 al., 2018) or by changes in the dislocation line direction (Pollet-Villard et al., 2016b). In
710 addition, the rate at the edges also increases comparatively more than the rate at the faces at pH
711 4.0 rather than at pH 4.5 (Figure 12b,c and Figure 11c,d), supporting that the contribution of the
712 different crystal patterns to dissolution might also be pH-dependent.

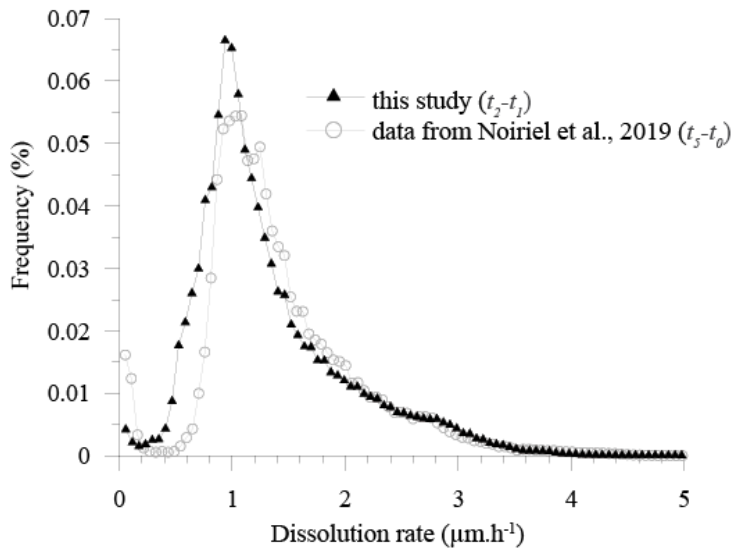
713 4.5. XMT dissolution rate distributions

714 The distributions of measured local dissolution rates, as shown in Figure 12, have an asymmetric
715 shape, bell-type with a long tail, similar to what has been reported for calcite in the literature
716 (Bibi et al., 2018; Brand et al., 2017; Fischer et al., 2012; Fischer et al., 2014; Noiriél et al.,
717 2019). However, contrary to the distributions obtained from VSI, AFM or DHM on single faces,
718 the distributions highlight here the contribution of all the crystal features to the dissolution
719 process, including the crystal edges and corners, cleavages, parting planes, macro-steps, etch
720 pits, flat $\{10\bar{1}4\}$ and misoriented surfaces, and topographic lows. However, it remains difficult
721 to evaluate precisely the contribution of each feature due to the impossibility to clearly define
722 their spatial extension, a soft transition being most likely observed between the edges, the faces
723 and/or the other crystal features instead.

724 Deconvoluting the rate distribution also assumes that the local rates would be constant through
725 time, a hypothesis not consistent with the experimental observations, e.g., the changes in the etch
726 pits-to-surface or edge-to-surface retreat ratios with time. Fischer and Lüttge, 2018 and Lüttge et
727 al., 2019 have previously pointed at the spatial and temporal variability in surface reactivity,
728 which should drive models of rate distribution to evolve to more probabilistic ones. These

729 models will appear to be well adapted to better constrain the dissolution process of crystals with
 730 different size, aspect ratio, density of defects at the surface and within the crystal, as all these
 731 parameters will contribute to modify the shape of the rate distribution. Indeed, a simple
 732 comparison of the local rate distribution for 11.1 h of experiment at pH 4.0 (i.e., between t_1 and
 733 t_2) with the results of Noiriel et al., 2019 after 12h of experiment in the same pH and
 734 experimental conditions shows that the rate distributions of the calcite crystals with two different
 735 aspect ratios do not match, although the rate at the peak maxima, the average rates (\bar{r}'_{diss} equal to
 736 $1.43 \mu\text{m}\cdot\text{h}^{-1}$ in Noiriel et al., 2019 vs $1.34 \mu\text{m}\cdot\text{h}^{-1}$ in this study), and maximum rates at the edges
 737 fit very well (Figure 15).

738



739

740 Figure 15. Normalized histograms for two calcite crystals with different aspect ratios dissolved
 741 in similar experimental conditions (i.e., pH 4.0, $\Delta t = 11.5 \text{ h} \pm 0.5 \text{ h}$). See Noiriel et al., 2019 for
 742 more details about the geometry of the second crystal. Note that the image processing procedure
 743 to evaluate surface retreat was different in the two studies, so that the rates at the edges from
 744 Noiriel et al., 2019 should be slightly higher if the surface retreat was calculated normal to
 745 surface instead of normal to the closest $\{10\bar{1}4\}$ surface only.

746

747 4.6. Does XMT have the ability to reconcile dissolution rates in the laboratory?

748 Compared to published data obtained in the same pH range (Figure 16), the average surface
749 normalized rates (Table 2) obtained with XMT are shown to be intermediate between the rates
750 determined on calcite powders (Chou et al., 1989; Plummer et al., 1978) and the rates derived
751 from AFM (De Giudici, 2002; Shiraki et al., 2000). The best agreement with previous studies
752 corresponds to the rates obtained on macro-crystals (i.e., cm-size crystals) (Busenberg and
753 Plummer, 1986; Sjöberg and Rickard, 1984, Schott et al., 1989), or from calcium released during
754 dissolution of cleaved crystals of 2-3 mm in dimension and epoxy-resined to a glass base
755 (Shiraki et al., 2000). The discrepancies between the rates are certainly explained by: (i) the
756 procedure of normalization, and (ii) differences in experimental preparation and setup, as already
757 discussed by Arvidson et al., 2003

758 A basic trend in the literature is confirmed that measured surface-normalized rates decrease as
759 spatial resolution improves and the field of view decreases (Figure 16). Considering geometric
760 surface area as the normalization factor, these differences could be easily related to the spatial
761 resolution of the imaging techniques, as the surface area scales with the resolution. Indeed, a
762 finer resolution catches up more details of the surface topography, in relation with the surface
763 roughness. This assumption is valid if we consider that the rates reported for the crystal used in
764 this study are at least 1.6 times higher compared to the rates that would be determined on
765 equivalent macro-crystals for which the contribution of edges and corners to the overall
766 dissolution should be minimal. However, in this case, it would not explain why our results agree
767 quite well rates obtained on macro-crystals (Busenberg and Plummer, 1986; Sjöberg and
768 Rickard, 1984, Schott et al., 1989), unless if we consider that normalization to a simple,
769 geometric surface area calculated from the dimension and shape of the unreacted crystals could
770 also lead to slight overestimation of the rates in experiments on macro crystals.

771 Of note, this scale-dependence of the surface area should not apply for rates determined from
772 powder experiments which results are normalized to the BET surface area (Brunauer et al., 1938)
773 instead. Some studies have reported BET surfaces areas about 2.5-3 times greater than geometric
774 surface area for calcite crystals in the range 20-53 μm , 10-100 μm or 355-500 μm (Naviaux et
775 al., 2018; Noiriél et al., 2019). In these experiments, in addition, the rates are normalized to the
776 surface area determined on unreacted minerals, whereas surface area is a dynamic parameter that

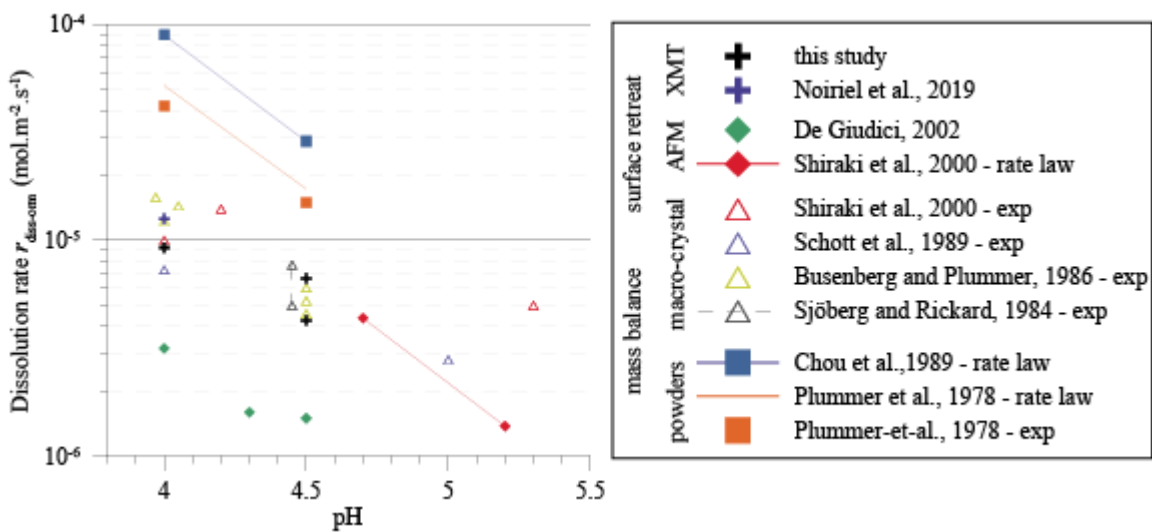
777 evolves as the reaction progresses (Noiriel and Daval, 2017). The scale-dependence does not
778 apply either for rates derived from direct measurements of the retreat velocity ($\mu\text{m}\cdot\text{h}^{-1}$) with
779 AFM, VSI, DHM or XMT (\bar{r}'_{diss}), for which the rates are further normalized to the molar volume
780 of the mineral, using Eq. 6. This method of normalization should be preferred, as it makes it
781 possible to overcome the issues inherent to surface normalization by the geometric or the BET
782 surface area. In this study, the rates normalized to the geometric surface area (\bar{r}_{diss}) slightly differ
783 from the rates derived from the retreat velocity (\bar{r}'_{diss}) (Table 2), but remains in quite good
784 agreement, thus indicating that the geometric surface area derived from XMT at the μm -scale
785 provides reliable estimation of the reactive surface area.

786 It is worth noting that normalization to the BET surface area would have reduced the rates by a
787 factor of 2.7. Nevertheless, it is surprising that the rate laws obtained by Plummer et al., 1978
788 and Chou et al., 1989, which were derived from powder experiments (with crystal size in the
789 range 177-420 μm , 420-841 μm , or 300-400 μm) and normalized to the geometric surface area
790 are so high compared to the rate determined with XMT on crystals of comparable size (Figure
791 16). Simple geometric considerations can show that the methods of normalization cannot account
792 for such discrepancies, as for instance the specific surface area value of $44.5 \text{ cm}^2\cdot\text{g}^{-1}$ used by
793 Plummer et al., 1978 for their 420-841 μm crystal size fraction fits well with our data.

794 As a consequence, the discrepancies must result from the sample preparation and/or from the
795 experimental conditions. Indeed, crushed material will exhibit more surface micro-defects,
796 micro-cracks, macro-steps, cleavages, parting planes, misoriented faces, and corners. Decreasing
797 the size fraction by increasing the crushing intensity will increase the density of these features as
798 well, thus promoting larger dissolution rates through a microstructural control of mineral
799 reactivity. The presence of fine size particles not removed by sieving or acid washing could be
800 an additional source of reactivity. In addition, contribution from the edges and corners to the
801 dissolution rate will be enhanced as far as the size fraction decreases (Figure 14c) by increasing
802 the population of kink and step edge sites (Lüttge et al., 2013; Briese et al., 2017), thus also
803 explaining larger rates compare to the XMT results. More importantly, the high stirring rates in
804 the experiment of Chou et al., 1989 and Plummer et al., 1978 should contribute, as an extrinsic
805 factor, in increasing the rates through transport control. For instance, Plummer et al., 1978

806 observed that, at pH 4, the rates were almost doubled between 800 and 1500 rpm. Similarly,
 807 Sjöberg and Rickard, 1984 observed, at pH 4.5, that the dissolution rate of a rotating macro-
 808 crystal was increased by a factor of 1.5 between 200 and 400 rpm (Figure 16). Taken together,
 809 these various processes account for the discrepancies between the crystal powder experiments of
 810 Chou et al., 1989; Plummer et al., 1978 and the higher rates derived from XMT.

811 Similarly, face-specific (i.e., with little or no contribution of the edges) rates derived from AFM,
 812 VSI or DHM on small portions of flat surfaces with lower reactivity (Dove and Platt, 1996) will
 813 exhibit lower rates compared to the overall rate of crystals determined by other methods. For
 814 instance, Shiraki et al., 2000 observed, during dissolution of cleaved crystal of 2-3 mm in
 815 dimension and the sides of which were epoxy-coated, that the calcium fluxes normalized to the
 816 geometric surface were about a factor of 3 higher than the rates determined by AFM at all pH
 817 values. In addition, ignoring the contribution of the edges will contribute to increasing the
 818 underestimation of the overall rates.



819
 820 Figure 16. Comparison between calcite dissolution rates (in HCl at pH 4-4.5) of the literature
 821 with this study. Both experimental data (exp) and derived models (rate law) are depicted. Rates
 822 are derived either from mass balance for crystal powders or cleaved macro-crystals of mm- to
 823 cm- size, or from surface retreat using AFM or XMT imaging.

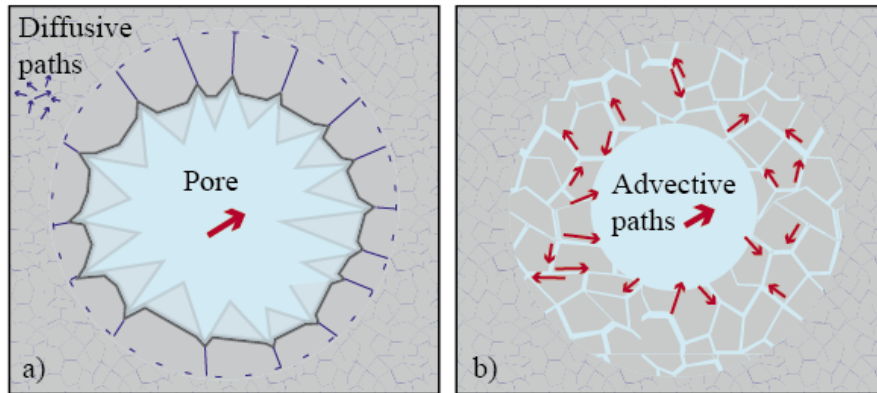
824

825 4.7. Implications for mineral reactivity in the environment

826 Although most studies on the effects of weathering or hydrothermal alteration on minerals have
827 focused on pit formation and morphology at the mineral surface (Berner et al., 1980; Velbel,
828 2009), several observations also mention the rounding of crystal edges in natural weathered
829 rocks (e.g., Velbel, 2009; Zhu et al., 2006) or experimentally altered crystals (e.g., Hellmann et
830 al., 2010; Iwasaki and Sano, 1997; Saldi et al., 2017), supporting the idea that the edges will play
831 a non-negligible role in the mass balance of alteration in various geochemical conditions. It is
832 interesting to note that the geometry of altered grains will reflect the influence of the free energy
833 of reaction ΔG_r . For instance, Hellmann et al., 2010 observed for albite that geometric etch pits
834 and angular edges formed below a critical value of free energy of reaction ($\Delta G_r < \Delta G_r^{crit}$),
835 whereas irregular pitting and rounded edges were observed at conditions $\Delta G_r > \Delta G_r^{crit}$. For
836 calcite, no pit formation is expected above a critical undersaturation ($\Omega > 0.41-0.54$, Teng,
837 2004), so that the crystal edges should be assumed to play a major role in global calcite reactivity
838 near equilibrium.

839 From a geologic perspective, the observations of higher crystal edge and corner reactivity in
840 calcite have also far-reaching implications for reactive transport in carbonate reservoirs or
841 aquifers, as geochemical reactivity should be linked to the rock fabric. Indeed, after carbonate
842 diagenesis (e.g., burial, marine or meteoric diagenesis), it is common to observe coatings of
843 fibrous, bladed or equant spar cements around grains (e.g., Flügel, 2010; Scholle and Ulmer-
844 Scholle, 2006), whose crystal edges and corners are directly in contact with advective fluids.
845 Preferential dissolution at the edges and corners of these cements could rapidly lead to pore
846 roughness decrease (Figure 17a), thus affecting the rock permeability (e.g., Noiriél et al., 2005;
847 Noiriél et al., 2016). Conversely, for encasing cements, e.g. drusy mosaic of equant spar, the
848 whole perimeter edge of the crystals (i.e., the grain boundaries) is in contact with fluids. It could
849 be advocated that transport would remain long diffusion-limited in this micro-porous network
850 compare to larger pores where transport is advective, but if dissolution is favored at the crystal
851 edges, and considering that corners and edges form the primary interconnected flow paths in
852 many rocks (Lee et al., 1991), this also could enhance the creation of new flowpaths along the
853 crystal edges (Figure 17b), thus explaining why the global reactivity can be rapidly increased in

854 some limestone, as shown for instance in the reactive flow experiment of Noiriel et al., 2009. As
855 a consequence, the quantitative estimation of the reactivity of crystal edges and corners appears
856 as crucial data to upscale mineral reactivity in porous media, which may ultimately be used in
857 reactive transport codes to model the modification of rock geometry and fluid flow paths.



858
859 Figure 17. Possible effect of preferential dissolution at the crystal edges and corners in carbonate
860 rocks. (a) Pore roughness reduction due to preferential dissolution of coatings of equant spar
861 cement grown in a pore. (b) Increase of diffusivity in micro-porous encasing cement due to
862 preferential dissolution at the crystal edges.

863
864 5. CONCLUSION

865 Exploring the dissolution of a single crystal of calcite in full 3D at the sub-micron scale has
866 revealed how the constitutive elements of the crystal with higher kink and step densities, i.e. the
867 edges and corners, as well as the patterns resulting from sample crushing and size reduction, i.e.,
868 cleavages, parting planes, miscut r-plane faces or other surface defects are associated to faster
869 surface retreat, and so higher dissolution rates compared to those with low surface energy
870 morphologies, i.e. flat $\{10\bar{1}4\}$ surfaces and topographic lows.

871 Far from equilibrium and under acidic conditions, the highest rates measured at the crystal corner
872 and edges are up to 7.2 and 2.1 times higher in average than the average face retreat, resulting in
873 dissolution rate enhanced by a factor of at least ~ 1.6 compared to what would be a face-specific
874 dissolution ignoring the contribution of the edges. The crystal edges take progressively control of

875 the dissolution process, with trains of steps propagating and progressively invading the initially
876 well-cleaved $\{10\bar{1}4\}$ surfaces, thus obliterating the face-specific retreat, with the consequence of
877 pit progressive annihilation. The results clearly show that the crystal edges play a major role in
878 the dissolution process of sub-millimeter scale calcite crystals. The contribution of the edges to
879 dissolution will be even promoted as far as the crystal size decreases, thus explaining why
880 dissolution rates determined on crystal powders scale with the crystal size distribution decrease.
881 The results obtained from a simple geometric model generalize, at the sub-millimeter scale, the
882 results of Briese et al., 2017 on nm-scale cubic crystals obtained from KMC simulations. The
883 crystal aspect ratio is another parameter which should be considered, as the faces with the
884 shortest dimensions should also experience a greater contribution from the edges.

885 With the perspective of determining reliable rates, these results should have implications for
886 modeling of dissolution or reactive transport in well crystallized carbonates. The results also
887 demonstrate that, despite a lower resolution compared to other techniques measuring the surface
888 retreat, XMT is very well adapted to evaluate the contribution of any of the different patterns that
889 are heterogeneously distributed at the crystal surface and through depth in course of dynamic
890 experiments and for different fluid compositions, both on the long term and independently of the
891 surface geometry or orientation. All considered, XMT appears to be helpful to provide reliable
892 reaction rates and to fill the gap between fine-scale (nm- to μm -scale) measurements of surface
893 reactivity and macroscopic determination of rates, a first necessary step toward bridging the gap
894 between field and laboratory rates. Our study has shown that ignoring the contribution of the
895 crystal edges as well as increasing the number of defects of higher reactivity via crushing at the
896 surface compared to flat, well-cleaved or polished surfaces can be source of large discrepancies
897 between the different approaches adopted so far in the laboratory. The origin of the largest rates
898 determined from powder experiments –up to one order of magnitude–, however, is not fully
899 resolved. In any case, it seems that these rates largely overestimate the reactivity of calcite at low
900 pH values.

901

902 TABLES

903 Table 1. Summary of the experimental conditions.

Stage	Time (h)	Duration (h)	pH	Flow rate Q (cm ³ ·h ⁻¹)	XMT imaging
t_0	0				×
t_1	8	8	4.5±0.1	8	×
t_2	19.1	11	4.0±0.1	8	×
t_3	22.1	3.1	4.5±0.1	8	×

904

905 Table 2. Summary of the experimental results obtained from XMT imaging and comparison
 906 with the rate obtained from chemistry

Stage	time (h)	pH	crystal volume (m ³)	% dissolved	crystal surface area (m ²)	r_{diss} (mol·s ⁻¹)	$r_{diss-norm}$ (mol·m ⁻² ·s ⁻¹)	\bar{r}'_{diss} (μm·h ⁻¹)	$\bar{r}'_{diss-norm}$ (mol·m ⁻² ·s ⁻¹)	$r_{diss-chem}$ (mol·s ⁻¹)
t_0	0		2.63×10^{-10}	0	3.12×10^{-6}					
t_1	8	4.5	2.49×10^{-10}	5.3	2.89×10^{-6}	1.28×10^{-11}	4.26×10^{-6}	0.59	4.43×10^{-6}	1.50×10^{-11}
t_2	19.1	4.0	2.13×10^{-10}	19.0	2.43×10^{-6}	2.46×10^{-11}	9.25×10^{-6}	1.34	1.01×10^{-5}	2.88×10^{-11}
t_3	22.1	4.5	2.07×10^{-10}	21.3	2.39×10^{-6}	1.61×10^{-11}	6.67×10^{-6}	0.94	7.11×10^{-6}	3.48×10^{-11}

907

908

909 FIGURES

910

911 AUTHOR INFORMATION

912 **Corresponding Author**

913 *e-mail:catherine.noiriel@univ-tlse3.fr

914

915 RESEARCH DATA

916 Details of analyses on aqueous samples and the 3D crystal geometry of the sub-sampled
917 volumes after segmentation can be found online at: <http://dx.doi.org/10.17632/hfg4w9hvs.w.1>

918

919 ACKNOWLEDGMENTS

920 This work was funded by the Institut Carnot ISIFOR under project SEQFRAC 400034. We
921 acknowledge the Paul Scherrer Institute for provision of synchrotron radiation beamtime at
922 Swiss Light Source, TOMCAT beamline X02DA. Local contacts David Haberthür and Iwan
923 Jerjen are acknowledged for their assistance with image acquisition. We also thank Thierry
924 Aigouy for assistance with SEM imaging.

925

926 REFERENCES

- 927 Akmal Butt, M. and Maragos, P., 1998. Optimum design of chamfer distance transforms. *Image*
928 *Processing, IEEE Transactions* **7**, 1477-1484.
- 929 Akutsu, N., 2014. Pinning of steps near equilibrium without impurities, adsorbates, or
930 dislocations. *Journal of Crystal Growth* **401**, 72-77.
- 931 Arvidson, R. S., Beig, M. S., and Lüttge, A., 2004. Single-crystal plagioclase feldspar dissolution
932 rates measured by vertical scanning interferometry. *Am. Miner.* **89**, 51-56.

- 933 Arvidson, R. S., Collier, M., Davis, K. J., Vinson, M. D., Amonette, J. E., and Lüttge, A., 2006.
934 Magnesium inhibition of calcite dissolution kinetics. *Geochim. Cosmochim. Acta* **70**,
935 583-594.
- 936 Arvidson, R. S., Evren Ertan, I., Amonette, J. E., and Lüttge, A., 2003. Variation in calcite
937 dissolution rates: A fundamental problem? *Geochim. Cosmochim. Acta* **67**, 1623-1634.
- 938 Berner, R. A., Sjöberg, E. L., Velbel, M. A., and Krom, M. D., 1980. Dissolution of pyroxenes
939 and amphiboles during weathering. *Science* **207**, 1205-1206.
- 940 Bibi, I., Arvidson, R. S., Fischer, C., and Luttge, A., 2018. Temporal evolution of calcite surface
941 dissolution kinetics. *Minerals* **8**, 256.
- 942 Bisschop, J., Dysthe, D. K., Putnis, C. V., and Jamtveit, B., 2006. In situ AFM study of the
943 dissolution and recrystallization behaviour of polished and stressed calcite surfaces.
944 *Geochim. Cosmochim. Acta* **70**, 1728-1738.
- 945 Bonzel, H. P., 2003. 3D equilibrium crystal shapes in the new light of STM and AFM. *Physics*
946 *Reports* **385**, 1-67.
- 947 Bouissonnié, A., Daval, D., Marinoni, M., and Ackerer, P., 2018. From mixed flow reactor to
948 column experiments and modeling: Upscaling of calcite dissolution rate. *Chem. Geol.*
949 **487**, 63-75.
- 950 Brand, A. S., Feng, P., and Bullard, J. W., 2017. Calcite dissolution rate spectra measured by in
951 situ digital holographic microscopy. *Geochim. Cosmochim. Acta* **213**, 317-329.
- 952 Bras, W. and Stanley, H., 2016. Unexpected effects in non crystalline materials exposed to X-ray
953 radiation. *Journal of Non-Crystalline Solids* **451**, 153-160.
- 954 Briese, L., Arvidson, R. S., and Luttge, A., 2017. The effect of crystal size variation on the rate
955 of dissolution : A kinetic Monte Carlo study. *Geochim. Cosmochim. Acta* **212**, 167-175.
- 956 Brunauer, S., Emmet, P. H., and Teller, E. A., 1938. Adsorption of gases in multimolecular
957 layers. *J. Am. Chem. Soc.* **60**, 309-319.
- 958 Busenberg, E. and Plummer, L. N., 1986. A comparative study of the dissolution and
959 precipitation kinetics of calcite and aragonite. In: Mumton, F. A. (Ed.), *Studies in*
960 *diagenesis, U. S. Geological Survey Bulletin*.
- 961 Chen, J. C., Reischl, B., Spijker, P., Holmberg, N., Laasonen, K., and Foster, A. S., 2014. Ab
962 initio Kinetic Monte Carlo simulations of dissolution at the NaCl-water interface.
963 *Physical Chemistry Chemical Physics* **16**, 22545-22554.
- 964 Chou, L., Garrels, R. M., and Wollast, R., 1989. Comparative study of the kinetics and
965 mechanisms of dissolution of carbonate minerals. *Chem. Geol.* **78**, 269-282.
- 966 Daval, D., Hellmann, R., Saldi, G. D., Wirth, R., and Knauss, K. G., 2013. Linking nm-scale
967 measurements of the anisotropy of silicate surface reactivity to macroscopic dissolution
968 rate laws: New insights based on diopside. *Geochim. Cosmochim. Acta* **107**, 121-134.
- 969 De Giudici, G., 2002. Surface control vs. diffusion control during calcite dissolution:
970 Dependence of step-edge velocity upon solution pH. *Am. Miner.* **87**, 1279-1285.
- 971 DePaolo, D. J. and Orr, F. M., 2008. Geoscience research for our energy future. *Physics Today*
972 **61**, 46-51.
- 973 Dove, P. M. and Platt, F. M., 1996. Compatible real-time reaction rates for in situ imaging of
974 mineral-water interactions using scanning force microscopy. *Chem. Geol.* **127**, 331-338.
- 975 Duckworth, O. W. and Martin, S. T., 2004. Dissolution rates and pit morphologies of rhomboedral
976 carbonate minerals. *Am. Miner.* **89**, 554-563.
- 977 Emmanuel, S., 2014. Mechanisms influencing micron and nanometer-scale reaction rate patterns
978 during dolostone dissolution. *Chem. Geol.* **363**, 262-269.

979 Fenter, P., Geissbühler, P., DiMasi, E., Strajer, G., Sorensen, L. B., and Sturchio, N. C., 2000.
980 Surface speciation of calcite observed in situ by high-resolution X-ray reflectivity.
981 *Geochim. Cosmochim. Acta* **64**, 1221-1228.

982 Fischer, C., Arvidson, R. S., and Lüttge, A., 2012. How predictable are dissolution rates of
983 crystalline material? *Geochim. Cosmochim. Acta* **98**, 177-185.

984 Fischer, C., Kurganskaya, I., Schaefer, T., and Lüttge, A., 2014. Variability of crystal surface
985 reactivity: What do we know? *Appl. Geochem.* **43**, 132-157.

986 Fischer, C. and Luttge, A., 2007. Converged surface roughness parameters - A new tool to
987 quantify rock surface morphology and reactivity alteration. *Am. J. Sci.* **307**, 955-973.

988 Fischer, C. and Luttge, A., 2018. Pulsating dissolution of crystalline matter. *Proceedings of the*
989 *National Academy of Sciences*.

990 Flügel, E., 2010. *Microfacies of Carbonate Rocks: Analysis, Interpretation and Application*.
991 Springer.

992 Godinho, J. R. A., Piazzolo, S., and Evins, L. Z., 2012. Effect of surface orientation on dissolution
993 rates and topography of CaF₂. *Geochim. Cosmochim. Acta* **86**, 392-403.

994 Gonzales, R. C. and Woods, R. E., 1992. *Digital image processing*. Addison-Wesley Publishing
995 Compagny, Reading, Massachusetts.

996 Hellmann, R., Daval, D., and Tisserand, D., 2010. The dependence of albite feldspar dissolution
997 kinetics on fluid saturation state at acid and basic pH: Progress towards a universal
998 relation. *Comptes Rendus Geoscience* **342**, 676-684.

999 Hillner, P. E., Gratz, A. J., Manne, S., and Hasma, P. K., 1992. Atomic-scale imaging of calcite
1000 growth and dissolution in real time. *Geology* **20**, 359-362.

1001 Hochella, M. F. J., 1990. Atomic structure, microtopography, composition and reactivity of
1002 mineral surfaces. In: Hochella, M. F. J. and White, A. W. Eds.), *Mineral-Water Interface*
1003 *Geochemistry*.

1004 Iwasaki, A. and Sano, T., 1997. Dissolution Behavior of Silicalite Crystal. *Zeolites* **19**, 41-46.

1005 Jordan, G. and Rammensee, W., 1998. Dissolution rates of calcite (10¹) obtained by
1006 scanning force microscopy: Microtopography-based dissolution kinetics on surfaces with
1007 anisotropic step velocities. *Geochim. Cosmochim. Acta* **62**, 941-947.

1008 Kump, L. R., Brantley, S. L., and Arthur, M. A., 2000. Chemical, weathering, atmospheric CO₂,
1009 and climate. *Annu. Rev. Earth Planet. Sci.* **28**, 611-667.

1010 Laanait, N., Callagon, E. B. R., Zhang, Z., Sturchio, N. C., Lee, S. S., and Fenter, P., 2015. X-
1011 ray-driven reaction front dynamics at calcite-water interfaces. *Science* **349**, 1330-1334.

1012 Lee, V. W., Mackwell, S. J., and Brantley, S. L., 1991. The Effect of Fluid Chemistry on Wetting
1013 Textures in Novaculite. *Journal of Geophysical Research* **96**, 10023-10037.

1014 Lüttge, A., Arvidson Rolf, S., Fischer, C., and Kurganskaya, I., 2019. Kinetic concepts for
1015 quantitative prediction of fluid-solid interactions. *Chem. Geol.* **504**, 216-235.

1016 Lüttge, A., Arvidson, R. S., and Fischer, C., 2013. A stochastic treatment of crystal dissolution
1017 kinetics. *Elements* **9**, 183-188.

1018 Lüttge, A., Winkler, U., and Lasaga, A. C., 2003. An interferometric study of dolomite
1019 dissolution: A new conceptual model for mineral dissolution. *Geochim. Cosmochim. Acta*
1020 **67**, 1099-1116.

1021 Maes, F., Collignon, A., Vandermeulen, D., Marchal, G., and Suetens, P., 1997. Multimodality
1022 image registration by maximization of mutual information. *IEEE Transactions on*
1023 *Medical Imaging* **16**, 187-198.

1024 Marone, F. and Stampanoni, M., 2012. Regridding reconstruction algorithm for real-time
1025 tomographic imaging. *Journal of Synchrotron Radiation* **19**, 1029-1037.

1026 Meijering, E. H. W., Niessen, W. J., and Viergever, M. A., 2001. Quantitative evaluation of
1027 convolution-based methods for medical image interpolation. *Medical image analysis* **5**,
1028 111-126.

1029 Miyata, K., Tracey, J., Miyazawa, K., Haapasilta, V., Spijker, P., Kawagoe, Y., Foster, A. S.,
1030 Tsukamoto, K., and Fukuma, T., 2017. Dissolution processes at step edges of calcite in
1031 water investigated by high-speed frequency modulation Atomic Force Microscopy and
1032 simulation. *Nano Letters* **17**, 4083-4089.

1033 Morse, J. W. and Arvidson, R. S., 2002. The dissolution kinetics of major sedimentary carbonate
1034 minerals. *Earth-Science Reviews* **58**, 51-84.

1035 Naviaux, J. D., Subhas, A. V., Rollins, N. E., Dong, S., Berelson, W. M., and Adkins, J. F., 2018.
1036 Temperature dependence of calcite dissolution kinetics in seawater. *Geochim.*
1037 *Cosmochim. Acta* **246**, 363-384.

1038 Noiriél, C., Bernard, D., Gouze, P., and Thibaut, X., 2005. Hydraulic properties and
1039 microgeometry evolution in the course of limestone dissolution by CO₂-enriched water.
1040 *Oil & Gas Science and Technology* **60**, 177-192.

1041 Noiriél, C. and Daval, D., 2017. Pore-scale geochemical reactivity associated with CO₂ storage:
1042 New frontiers at the fluid-solid interface. *Accounts of Chemical Research* **50**, 759-768.

1043 Noiriél, C., Luquot, L., Madé, B., Raimbault, L., Gouze, P., and van der Lee, J., 2009. Changes
1044 in reactive surface area during limestone dissolution: An experimental and modelling
1045 study. *Chem. Geol.* **265**, 160-170.

1046 Noiriél, C., Oursin, M., Saldi, G. D., and Haberthür, D., 2019. Direct determination of
1047 dissolution rates at crystal surface using 3D X-ray micro-tomography. *Earth and Space*
1048 *Chemistry* **3**, 101-108.

1049 Noiriél, C., Steefel, C. I., Yang, L., and Ajo-Franklin, J., 2012. Upscaling calcium carbonate
1050 precipitation rates from pore to continuum scale. *Chem. Geol.* **318-319**, 60-74.

1051 Noiriél, C., Steefel, C. I., Yang, L., and Bernard, D., 2016. Effects of pore-scale heterogeneous
1052 precipitation on permeability and flow *Adv. Water Resour.* **95**, 125-137.

1053 Parkhurst, D. L. and Appelo, C. A. J., 2013. Description of input and examples for PHREEQC
1054 version 3--A computer program for speciation, batch- reaction, one-dimensional
1055 transport, and inverse geochemical calculations, *Techniques and Methods 6-A43*,
1056 available only at <http://pubs.usgs.gov/tm/06/a43>. U.S. Geological Survey

1057 Pitas, I., 2000. *Digital image processing algorithms and applications*. Wiley.

1058 Plummer, L. N., Wigley, T. M. L., and Parkhurst, D. L., 1978. The kinetics of calcite dissolution
1059 in CO₂-water systems at 5° to 60°C and 0.0 to 1.0 atm CO₂. *Am. J. Sci.* **278**, 179-216.

1060 Pollet-Villard, M., Daval, D., Ackerer, P., Saldi, G. D., Wild, B., Knauss, K. G., and Fritz, B.,
1061 2016a. Does crystallographic anisotropy prevent the conventional treatment of aqueous
1062 mineral reactivity? A case study based on K-feldspar dissolution kinetics. *Geochim.*
1063 *Cosmochim. Acta* **190**, 294-308.

1064 Pollet-Villard, M., Daval, D., Fritz, B., Knauss, K. G., Schäfer, G., and Ackerer, P., 2016b.
1065 Influence of etch pit development on the surface area and dissolution kinetics of the
1066 orthoclase (001) surface. *Chem. Geol.* **442**, 148-159.

1067 Rickard, D. and Sjöberg, E. L., 1983. Mixed kinetic control of calcite dissolution rates. *Am. J.*
1068 *Sci.* **283**, 815-830.

- 1069 Ruiz-Agudo, E., Putnis, C. V., Jiménez-López, C., and Rodríguez-Navarro, C., 2009. An atomic
1070 force microscopy study of calcite dissolution in saline solutions: The role of magnesium
1071 ions. *Geochemica and Cosmochimica Acta* **73**, 3201-3217.
- 1072 Russ, J. C., 2011. *The Image Processing Handbook, Sixth Edition*. CRC Press, Boca Raton, FL.
- 1073 Saldi, G. D., Voltolini, M., and Knauss, K. G., 2017. Effects of surface orientation, fluid
1074 chemistry and mechanical polishing on the variability of dolomite dissolution rates.
1075 *Geochim. Cosmochim. Acta* **206**, 94-111.
- 1076 Scholle, P. A. and Ulmer-Scholle, D. S., 2006. *Color Guide to Petrography of Carbonate Rocks*.
1077 AAPG
- 1078 Schott, J., Brantley, S. L., Drear, D., Guy, C., Borcsik, M., and Willaime, C., 1989. Dissolution
1079 kinetics of strained calcite. *Geochim. Cosmochim. Acta* **53**, 373-382.
- 1080 Shiraki, R., Rock, P. A., and Casey, W. H., 2000. Dissolution kinetics of calcite in 0.1M NaCl
1081 solution at room temperature: An atomic force microscopic (AFM) study. *Aquatic*
1082 *Geochemistry* **6**, 87-108.
- 1083 Sjöberg, E. L. and Rickard, D. T., 1984. Calcite dissolution kinetics: Surface speciation and the
1084 origin of the variable pH dependence. *Chem. Geol.* **42**, 119-136.
- 1085 Smith, M. E., Knauss, K. G., and Higgins, S. R., 2013. Effects of crystal orientation on the
1086 dissolution of calcite by chemical and microscopic analysis. *Chem. Geol.* **360**, 10-21.
- 1087 Stampanoni, M., Groso, A., Isenegger, A., Mikuljan, G., Chen, Q., Bertrand, A., Henein, S.,
1088 Betemps, R., Frommherz, U., Böhler, P., Meister, D., Lange, M., and Abela, R., 2006.
1089 Trends in synchrotron-based tomographic imaging: the SLS experience *SPIE Optics +*
1090 *Photonics, 2006* San Diego, California, United States.
- 1091 Steefel, C. I., DePaolo, D. J., and Lichtner, P. C., 2005. Reactive transport modeling: An
1092 essential tool and a new research approach for the Earth sciences. *Earth Planet. Sci. Lett.*
1093 **240**, 539-558.
- 1094 Stipp, S. L. S., Eggleston, C. M., and Nielsen, B. S., 1994. Calcite surface observed at
1095 microtopographic and molecular scales with atomic force microscopy (AFM). *Geochim.*
1096 *Cosmochim. Acta* **58**, 3023-3033.
- 1097 Teng, H. H., 2004. Controls by saturation state on etch pit formation during calcite dissolution.
1098 *Geochim. Cosmochim. Acta* **68**, 253-262.
- 1099 Ueta, S., Satoh, H., Nishimura, Y., Ueda, A., and Tsukamoto, K., 2013. Dynamic and
1100 topographic observation of calcite dissolution using enhanced in-situ phase-shift
1101 interferometry. *Journal of Crystal Growth* **363**, 294-299.
- 1102 Velbel, M. A., 2009. Dissolution of olivine during natural weathering. *Geochim. Cosmochim.*
1103 *Acta* **73**, 6098-6113.
- 1104 Villanova, J., Daudin, R., Lhuissier, P., Jauffrès, D., Lou, S., Martin, C. L., Labouré, S.,
1105 Tucoulou, R., Martinez-Criado, G., and Salvo, L., 2017. Fast in situ 3D nanoimaging: A
1106 new tool for dynamic characterization in materials science. *Materials Today* **20**, 354-359.
- 1107 Xu, M., Hu, X., Knauss, K. G., and Higgins, S. R., 2010. Dissolution kinetics of calcite at 50-70
1108 °C: An atomic force microscopic study under near-equilibrium conditions. *Geochemica*
1109 *and Cosmochimica Acta* **74**, 285-4297.
- 1110 Zhu, C., Veblen, D. R., Blum, A. E., and Chipera, S. J., 2006. Naturally weathered feldspar
1111 surfaces in the Navajo Sandstone aquifer, Black Mesa, Arizona: Electron microscopic
1112 characterization. *Geochim. Cosmochim. Acta* **70**, 4600-4616.